CHAPTER IV

NUMERICAL RESULTS AND DISCUSSION

4.1 Convergence and Accuracy of Present Solution Scheme

The convergence and accuracy of the numerical solution scheme described in the previous chapter are investigated in this section. First of all , the convergence and stability of numerical solutions with respect to the following parameters are studied : (1) the upper limit of numerical integration, ξ_L , in eqn (2.14) used for determining the influence functions ; (2) the number of generalized coordinates, N ,used in the displacement function ,eqn(2.43) ; (3) the number of ring elements , M , used to discretize the circular area as shown in Fig.2.3 ; (4) the penalty number , λ .

Table 4.1 presents the convergence of nondimensional displacement , $a\mu w/P_0$, of a circular rigid plate subjected to a central load P_0 as shown in Fig. 4.1(a) with respect to ξ_L . The nondimensional time , $t^*=ct/a^2$, is used in the numerical study where c is given by eqn (2.9) . It can be seen from Table 4.1 that the accuracy of the present solution scheme improves with increasing ξ_L when compared to the numerical solution given by Yue and Selvadurai (1995) . For example , the difference from both solutions is approximately 30% for ξ_L=20 whereas , when ξ_L=80 , it is only about 1%. It is also noted that the solutions for all values of t^* are stable when ξ_L is larger than 80.

Table 4.2 shows the convergence and accuracy of the present solution scheme with respect to N and M by comparing with the finite element solution given by Small and Zhang (1994). Nondimensional displacement , $\mu w(0)/q_0 a$, and nondimensional

bending moment , $M_r(0)/q_0a^2$, for a uniformly loaded elastic plate resting on a poroelastic layer underlying by a rigid stratum are shown in Table 4.2(a) and 4.2(b) , respectively. The relative rigidity and Poisson's ratio of the plate are defined as Kr = $(E_p/E_h)(1-\nu^2)(t_p/a)^3$ = 1.0 and ν_p = 0.30 , respectively , where E_h denotes the modulus of elasticity of the layer . In addition , the thickness of the layer is equal to "a" , ν=0.0 and ν_u=0.50. Numerical results presented in Table 4.2 indicate that the number of generalized coordinates , N , and the number of ring elements , M , have a significant influence on the numerical stability and accuracy of the solutions. These results show rapid convergence with respect to displacement , but a slower convergence for bending moment . It is also found that the accurate computation of numerical solution requires $N\geq 6$ terms and $M\geq 20$, respectively . Similar convergence characteristics are also observed for a centrally loaded plate.

Table 4.3 presents the influence of the penalty number, λ , on numerical solutions for a centrally loaded circular elastic plate resting on the surface of a multi-layered poroelastic half-space as shown in Fig 4.1(c). A layered system consisting of two poroelastic layers bonded to an underlying poroelastic half-space is considered in the numerical study. The properties of the first layer are $B^{(1)} = 1.0, \nu^{(1)} = 0.25$ and $\nu_u^{(1)} = 0.50$; for the second layer, $B^{(2)} = 0.8, \nu^{(2)} = 0.25$ and $\nu_u^{(2)} = 0.35$ and for the underlying half-space , $B^{(3)} = 0.6, \nu^{(3)} = 0.2$ and $\nu_u^{(3)} = 0.3$. In addition , $\mu^{(2)}/\mu^{(1)} = 1$, $\mu^{(3)}/\mu^{(1)} = 2$, $\kappa^{(1)}/\kappa^{(2)} = 0.01$ and $\kappa^{(3)}/\kappa^{(2)} = 0.5$. The thickness of the first and the second layers are equal to "$2a$" and "a" , respectively. Nemurical results are presented for Kr = 0.5 to 1000 and $t^* = 10^4$, 1, 10^{-4} where $t^* = c^{(2)}t/a^2$ ($c^{(2)}$ is given by eqn(2.9) inwhich the superscript (2) denotes the second layer of the half-space). It can be seen from Table 4.3 that the solution is stable within the range $10^{-4} \leq \lambda \leq 10^{-1}$. The solutions presented in Table 4.3 confirm that there is a wide range of λ values within which the solution scheme is extremely stable. It is also seen that bending moment at the edge of plate obtained from the solution are nearly zero for the range of $10^{-4} \leq \lambda \leq 10^{-1}$. This also confirms that the present scheme is capable of satisfying the

required plate edge boundary conditions with high accuracy within the range $10^{-4} \leq \lambda \leq 10^{-1}$.

The comparison of solutions from the present study with the numerical solutions given by Yue and Selvadurai(1995) is shown in Fig 4.2 . This figure shows time histories of nondimensional displacement for a centrally loaded circular rigid plate resting on the surface of a homogeneous poroelastic half-space. The seven sets of Poisson's ratios are considered in the numerical study , i.e., $\nu_u = 0.5$; ν =0.0 , 0.20 , 0.40, 0.49 and $\nu = 0.0$; ν_u =0.01 , 0.20 , 0.40. In addition, B=1.0 . It is evident from the figure that both solutions show very good agreement in all sets of solutions with the difference being less than 1.0%.

Figures 4.3(a) and 4.3(b) present the comparison between the contact stress profiles computed from eqn(2.69) and those reported by Browicka(1939) and Brown(1969) , respectively , for different Kr. Browicka(1939) and Brown(1969) presented the contact stress distribution for a centrally loaded and a uniformly loaded circular plate (ν_p=0.30) resting on a surface of an ideal elastic half-space (ν=0.25) , respectively. Close agreement between the solutions is observed for both flexible and relatively rigid plates.

4.2 Quasi-Static Behaviour of Circular Plate on Multi-Layered Poroelastic Half-Space

Numerical solutions presented in the preceding section confirm the convergence , numerical stability and accuracy of the present solution scheme. In this section , the quasi-static response of a circular elastic plate resting on a multi-layered poroelastic half-space is investigated . A layered system consisting of two poroelastic layers bonded to an underlying poroelastic half-space , as shown in Fig 4.4 , is considered in all numerical studies. The properties of the second layer are

$B^{(2)} = 0.8, \nu^{(2)} = 0.25$ and $\nu_u^{(2)} = 0.35$ and for the underlying half-space , $B^{(3)} = 0.6, \nu^{(3)} = 0.2$ and $\nu_u^{(3)} = 0.3$. In addition , $B^{(1)} = 1.0$, $\mu^{(2)}/\mu^{(1)} = 1.0$, $\mu^{(3)}/\mu^{(1)} = 2.0$ and $\kappa^{(3)}/\kappa^{(2)} = 0.5$. These properties are considered as constants throughout this study while the properties of the first layer and the circular plate are varied in order to investigate their effect on the flexural behaviour of the plate.

4.2.1 Centrally loaded Circular Plate

a) Influence of Relative Rigidity of Plate

The time histories of nondimensional displacement , $a\mu^{(1)}w/P_0$, and nondimensional bending moment, M_r/P_0a , for a centrally loaded circular elastic plate (ν_p =0.3) resting on the surface of a multi-layered poroelastic half-space ($\nu^{(1)}$=0.25 , $\nu_u^{(1)}$=0.50 , $\kappa^{(1)}/\kappa^{(2)}$=0.01 and the thickness of the first layer , h1/a=2.0), as shown in Fig 4.4(a) , are studied from Fig 4.5 to Fig 4.7. The seven values of Kr (Kr = 0.5, 1, 5, 10, 50, 100, 500) and the nondimensional time , $t^*=c^{(2)}t/a^2$, are considered in the numerical study. The actual time , t , can be determined if the properties of soil medium are given. For example , the properties of soil are assumed to be B=1.0 , ν=0.30 , ν_u=0.50 and μ=2.62x10^5 kN/m^2 , respectively. In addition , κ = k/γ_w =1.02x10^{-10} m^4/kN.s since k$\leq$10^{-9} m/s for clay and γ_w = 9.81 kN/m^3 for water. From eqn(2.9) and the above soil properties , c is equal to 93.534x10^{-6} m^2/s. If the radius of plate is equal to 2.0 m then the final solution (i.e. when t^* = 10^4) is reached at t = (10^4 x 2^2 / 93.534x10^{-6}) / (60 x 60 x 24 x 365) = 13.56 years.

Figure 4.5 presents the time histories of nondimensional displacement of a centrally loaded plate in the range of $10^{-4} \leq t^* \leq 10^4$. It is found that the values of Kr have no effect on the rate of consolidation of plate but have a significant influence effect on the magnitude of the plate displacement . It also indicates that the displacements decrease with increasing the value of Kr for all values of t^*.

Final solutions of displacement and bending moment profiles for different values of Kr are shown in Fig 4.6 and 4.7 , respectively. It can be seen from Fig 4.6 that for Kr>50 the solution converges toward the value corresponding to an infinitely rigid plate. It is found from Fig 4.7 that the magnitude of nondimensional moment increases with increasing the value of Kr and shows discontinuity of moment at r=0. The gradient of moment profiles rapidly increases from r=0.5a to r=0 and its magnitude approaches infinity at the vicinity of the plate origin. It also shows that the moment at the edge of all plates are nearly zero . This corresponds to the case where Kirchhoff boundary conditions given by eqns (2.58) and (2.59) are imposed along the plate edge.

b) Influence of Drained and Undrained Poisson's Ratios

The influence of drained and undrained Poisson's ratio of the first layer , $\nu^{(1)}$ and $\nu_u^{(1)}$, on the nondimensional central displacement , $a\mu^{(1)}w(0)/P_0$, and nondimensional bending moment at r=0.5a , $M_r(0.5a)/P_0a$, of a centrally loaded circular elastic plate (ν_p =0.3 , Kr=0.5) are investigated from Fig 4.8-4.11. The four sets of Poisson's ratios of the first layer are considered in the numerical studies ($\nu_u^{(1)}$ = 0.5 ; $\nu^{(1)}$ =0.0 , 0.20 , 0.40, 0.49 for Fig 4.8 and 4.9 and $\nu^{(1)}$ = 0.0 ; $\nu_u^{(1)}$ =0.0 , 0.01 , 0.20 , 0.40 , 0.50 for Fig 4.10 and 4.11). In addition , $\kappa^{(1)}/\kappa^{(2)}$=0.01 and h1/$a$=2.0 .

Time histories of central displacement and bending moment at r=0.5a for different values of drained Poisson's ratio of the first layer are shown in Fig 4.8 and 4.9 , respectively. It can be seen from both figures that the value of $\nu^{(1)}$ has a significant influence on both the magnitude and rate of consolidation of the plate. The numerical results in Fig 4.8 show identical initial displacement for all sets of Poisson's ratios. The rate of consolidation at any times increases with increasing in the value of $\nu_u^{(1)} - \nu^{(1)}$

and has its maximum value when $\nu_u^{(1)} = 0.50$ and $\nu^{(1)} = 0.0$. Similar results are also observed for the nondimensional bending moment shown in Fig 4.9. This is the consequence of the fact that the undrained behaviour of poroelastic materials is mainly governed by the undrained Poisson's ratio, therefore a higher value of $\nu_u^{(1)} - \nu^{(1)}$ means a lesser undrained compressibility of the layer system.

Figures 4.10 and 4.11 present time histories of central displacement and bending moment at r=0.5a , respectively , for different values of undrained Poisson's ratio of the first layer. It is found that the numerical results show identical final displacement and moment for all sets of the undrained Poisson's ratios and the rate of consolidation at any times increases with the increases in $(\nu_u^{(1)} - \nu^{(1)})$. These behaviours are due to the fact that at final condition the drained behaviour is governed by the drained Poisson's ratio. It also can be seen from Fig 4.8 - 4.11 that when $\nu \rightarrow \nu_u$ the numerical solutions shows identical results at all values of time. This is the consequence of the fact that when $\nu \rightarrow \nu_u$ the poroelastic materials exhibit only an elastic deformation and the consolidation effects are absent .

c) Influence of Layer Permeability

The influence of layer permeability on the nondimensional central displacement and nondimensional moment at r=0.5a of a centrally loaded circular elastic plate (ν_p =0.3 , Kr=0.5) is considered in Fig 4.12 and Fig 4.13 , respectively , by setting $\nu^{(1)}$=0.25 , $\nu_u^{(1)}$=0.50 , h1/a=2.0 and $\kappa^{(1)} / \kappa^{(2)}$ = 0.001 , 0.01 , 0.1 , 1.0 and 10. It can be seen from these two figures that the ratio $\kappa^{(1)} / \kappa^{(2)}$ has a significant influence on the flexural behaviour on of the plate. The consolidation settlement of the plate is first noted in the case of $\kappa^{(1)} / \kappa^{(2)}$=10 whereas , for $\kappa^{(1)} / \kappa^{(2)}$=0.001 , it is observed when $t^* \geq 0.1$. The earliest final solution is reached for $\kappa^{(1)} / \kappa^{(2)}$=10 and the latest for $\kappa^{(1)} / \kappa^{(2)}$=0.001. This behaviour is due to the fact that the first layer is less permeable in the latter case. Comparison of the results presented in Fig 4.12 and 4.13 indicates

that the variation of the ratio $\kappa^{(1)} / \kappa^{(2)}$ essentially results in a shift of the solution profiles in the time scale. The numerical results in Fig.4.12 and 4.13 show identical initial and final solutions since the material parameters ν , ν_u , μ and the thickness of the two layers are the same for all values of $\kappa^{(1)} / \kappa^{(2)}$.

d) Influence of Layer Thickness

The influence of layer thickness on the nondimensional displacement and nondimensional moment are presented in Fig. 4.14 and 4.15, respectively, for five different values of the thickness of the first layer , i.e. h1/a=0.20 , 0.40 , 1.0 , 1.40 and 1.80 . Note that the total thickness of the two layers is $2a$, $\nu^{(1)}$=0.25 , $\nu_u^{(1)}$=0.26 , $\kappa^{(1)}/\kappa^{(2)}$=0.01 . It is evident that the initial solutions of the plate (ν_p =0.3 , Kr=0.5) for different values of h1/a are different and their order of magnitude is identical to that of h1/a. This is due to the fact that the undrained behaviour of the plate-multi-layered half-space system is mainly governed by undrained Poisson's ratio. The lower value of h1/a means the lesser undrained compressibility of the multi-layered medium since $\nu_u^{(1)} < \nu_u^{(2)}$. It is also found that the final solutions of the plate are also identical for all values of h1/a since the elastic properties (drained) of different layered systems are identical .

e) Contact Stress Profile

The contact stress profiles , $T_z(r,t).a^2/P_0$, of a centrally loaded elastic plate (ν_p=0.30) on a multi-layered poroelastic half-space , as shown in Fig. 4.4(a) , for different Kr and t^* are presented in Fig. 4.16(a) to 4.16(d). The properties of a multi-layered poroelastic half-space are $\nu^{(1)}$=0.25 , $\nu_u^{(1)}$=0.50 , $\kappa^{(1)}/\kappa^{(2)}$=0.01 and h1/$a$=2.0. It can be seen that the magnitude of contact stress at center of plate decreases but increases at the plate edge when the value of Kr increases. The magnitude of the

solution at center of plate is larger than the solution at the plate edge when the plate is flexible but in the case of a rigid plate the solution at the edge of plate becomes larger. It is noted that the contact stress profiles are independent of time when the plate is almost rigid.

4.2.2 Uniformly Loaded Circular Plate

The influence of various parameters on the quasi-static response of a centrally loaded circular elastic plate is studied in the preceding section. In this section, the effect of those parameters on the flexural behaviour of a uniformly loaded circular elastic plate is investigated.

The influence of relative rigidity , Kr , on nondimensional displacement , $\mu^{(1)}w(r)/q_0a$, and nondimensional moment , $M_r(r)/q_0a^2$, of a uniformly loaded circular plate as shown in Fig 4.4(b) are investigated in Fig 4.17 and 4.18 , respectively . The properties of a multi-layered poroelastic half-space are $\nu^{(1)} = 0.25$, $\nu_u^{(1)} = 0.50$, $\kappa^{(1)}/\kappa^{(2)} = 0.01$ and $h1/a = 2.0$. The seven values of Kr (Kr = 0.5, 1, 5, 10, 50, 100, 500) are employed in the numerical study. It is found from Fig 4.17 that the displacement increases at the plate edge but decreases at the center of the plate when the value of Kr increases. This is due to the fact that when Kr is increased , the plate is more rigid . This results in the contact stress to be distributed from the origin to the edge of plate more than in the case of a flexible plate. Therefore , the displacement at the edge of plate becomes increasing since the displacement of plate depends on the normal stress along the contact surface.

Figure 4.18 shows the final solutions of bending moment profiles for different values of Kr . Unlike in the case of a centrally loaded plate , as shown in Fig 4.4(a) , the moment profiles do not show the discontinuity. It is found that the bending moments increase with increasing Kr and the maximum values occur at the center of

the plate. In addition , the moment is nearly zero at the edge of the plate due to Kirchhoff boundary conditions as in the case of a centrally loaded plate.

Figures 4.19 and 4.20 present the effect of permeability on nondimensional displacement and nondimensional bending moment of a uniformly loaded circular elastic plate resting on a surface of multi-layered poroelastic half-space. The half-space is considered by setting $\nu^{(1)}$=0.25 , $\nu_u^{(1)}$=0.50 , h1/a=2.0 and $\kappa^{(1)} / \kappa^{(2)}$ = 0.001 , 0.01 , 0.1 , 1.0 and 10 , respectively. It can be seen that the results are similar to the study in the case of a centrally loaded plate. The results indicate that the variation of the ratio $\kappa^{(1)} / \kappa^{(2)}$ results in a shift of the solution profiles in the time scale.

Figure 4.21 shows the comparison of final solution of displacement profile between the plate (ν_p=0.3) subjected to uniformly distributed load, q_0, and concentrated load, $P_0=q_0\pi a^2$ for various value of Kr. The properties of a multi-layered poroelastic half-space are $\nu^{(1)}$=0.25 , $\nu_u^{(1)}$=0.50 , $\kappa^{(1)}/\kappa^{(2)}$=0.01 and h1/$a$=2.0. It is evident that the difference of maximum displacement for both cases decreases with increasing the value of Kr. It is also found that for Kr≥50 the displacement of the plate for both cases are very close and converge to the value corresponding to an infinitely rigid plate.

The contact stress profiles , $T_z(r,t)/q_0$, of a uniformly loaded elastic plate (ν_p=0.30) on a multi-layered poroelastic half-space , as shown in Fig. 4.4(b) , for different Kr and t^* are presented in Fig. 4.22(a) to 4.22(d). The properties of a multi-layered poroelastic half-space are $\nu^{(1)}$=0.25 , $\nu_u^{(1)}$=0.50 , $\kappa^{(1)}/\kappa^{(2)}$=0.01 and h1/$a$=2.0. The magnitude of contact stress at center of the plate decreases but increases at the plate edge when the value of Kr increases as in the case of a centrally loaded plate. However , the solutions in Fig. 4.22(a) to 4.22(d) at the plate edge are larger than the solution at the center of the plate for both flexible and relatively rigid plates. Once again , the contact stress profiles are nearly independent on time for all values of Kr.

Table 4.1 : Convergence and comparison of nondimensional displacements of centrally loaded circular rigid plate on homogeneous poroelastic half-space for different values of ξ_L (M=20 , λ=0.01, B=1.0, ν=0.10 , ν_u=0.50)

t^*	Present study with different ξ_L						Yue & Selvadurai (1995)
	ξ_L= 20	ξ_L= 40	ξ_L= 60	ξ_L= 80	ξ_L= 100	ξ_L=120	
0.04	0.137	0.149	0.160	0.152	0.152	0.152	0.152
0.16	0.227	0.173	0.177	0.169	0.169	0.169	0.168
0.36	0.105	0.172	0.188	0.180	0.180	0.180	0.180
0.64	0.122	0.182	0.195	0.187	0.187	0.187	0.188
1.00	0.202	0.170	0.201	0.192	0.192	0.192	0.194
1.44	0.137	0.205	0.205	0.196	0.196	0.196	0.199
1.96	0.173	0.711	0.208	0.200	0.199	0.200	0.202

Table 4.2 : Convergence and comparison of solutions with N and M for a uniformly loaded circular elastic plate on poroelastic layer with rigid base (λ=0.01, t^*=10 , ν_p=0.30 , Kr=0.50 , B=1.0, ν=0.10 , ν_u=0.50)

(a) Nondimensional displacement , $\mu w(0)/q_0 a$

N	Present study with different N and M				Small & Zhang (1994)
	M=5	M=10	M=20	M=30	
2	0.393	0.390	0.388	0.387	
4	0.405	0.403	0.401	0.400	0.399
6	0.404	0.402	0.400	0.400	

(b) Nondimensional moment , $M_r(0)/q_0 a^2$

N	Present study with different N and M				Small & Zhang (1994)
	M=5	M=10	M=20	M=30	
2	0.016	0.021	0.023	0.024	
4	0.034	0.041	0.043	0.045	0.039
6	0.030	0.037	0.040	0.041	

Table 4.3 : Convergence of solution with penalty number for a centrally loaded plate on a multi-layered poroelastic half-space

($\nu_p = 0.30$, $B^{(1)}=1.0$, $\nu^{(1)}=0.25$, $\nu_u^{(1)}=0.5$, $\kappa^{(1)}/\kappa^{(2)}=0.01$, $h^{(1)}/a=2.0$)

t^*	λ	$a\,\mu^{(1)}w(0)/P_0$			$M_r(0.5a)/P_0a$			$M_r(a)/P_0a$		
		K_r=0.50	K_r=2.00	K_r=100	K_r=0.50	K_r=2.00	K_r=100	K_r=0.50	K_r=2.00	K_r=100
10^{-4}	10^{-4}	0.2408	0.1582	0.1124	0.0051	0.0245	0.0374	0.0001	0.0000	-0.0002
	10^{-2}	0.2409	0.1582	0.1124	0.0051	0.0245	0.0374	0.0001	0.0002	0.0001
	10^{-1}	0.2409	0.1582	0.1124	0.0051	0.0245	0.0374	-0.0001	0.0003	-0.0001
	1	0.2408	0.1582	0.1124	0.0054	0.0247	0.0374	0.0061	0.0010	0.0001
	10^{2}	0.2381	0.1582	0.1124	-0.0002	0.0249	0.0374	-0.0969	0.0094	0.0002
	10^{4}	0.2619	0.1591	0.1124	-0.0029	0.0242	0.0350	-0.0115	-0.0361	-0.6893
1	10^{-4}	0.2604	0.1711	0.1257	0.0077	0.0251	0.0354	0.0001	0.0000	-0.0004
	10^{-2}	0.2604	0.1711	0.1257	0.0077	0.0251	0.0354	0.0003	0.0001	0.0002
	10^{-1}	0.2604	0.1711	0.1257	0.0078	0.0251	0.0354	0.0010	0.0001	0.0001
	1	0.2604	0.1711	0.1257	0.0080	0.0251	0.0353	0.0014	0.0004	0.0001
	10^{2}	0.2608	0.1711	0.1257	0.0075	0.0265	0.0352	0.0118	0.0309	-0.0018
	10^{4}	0.2606	0.1684	0.1257	0.0261	0.0214	0.0346	-0.0628	0.0075	0.0632
10^{4}	10^{-4}	0.3163	0.2166	0.1681	0.0115	0.0283	0.0376	0.0001	-0.0003	-0.0001
	10^{-2}	0.3163	0.2166	0.1681	0.0115	0.0283	0.0376	-0.0001	0.0000	0.0003
	10^{-1}	0.3163	0.2166	0.1681	0.0115	0.0283	0.0376	0.0013	0.0002	0.0001
	1	0.3163	0.2166	0.1681	0.0110	0.0284	0.0376	-0.0097	0.0014	0.0002
	10^{2}	0.3157	0.2164	0.1681	0.0126	0.0206	0.0374	-0.0144	0.8981	-0.0030
	10^{4}	0.3167	0.2171	0.1681	0.0027	0.0359	0.0382	-0.0625	0.0298	-0.0019

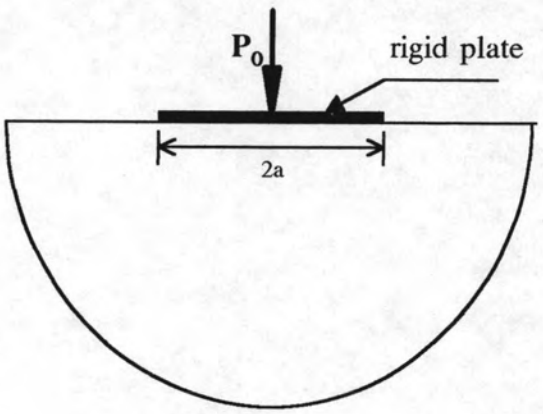

(a) Homogeneous poroelastic half-space

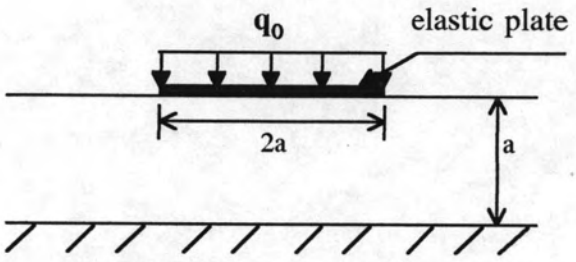

(b) Poroelastic layer with rigid base

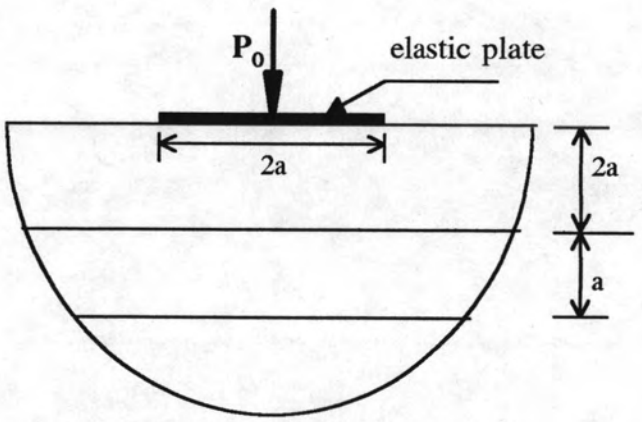

(c) Multi-layered poroelastic half-space

Figure 4.1 : System considered in section 4.1.

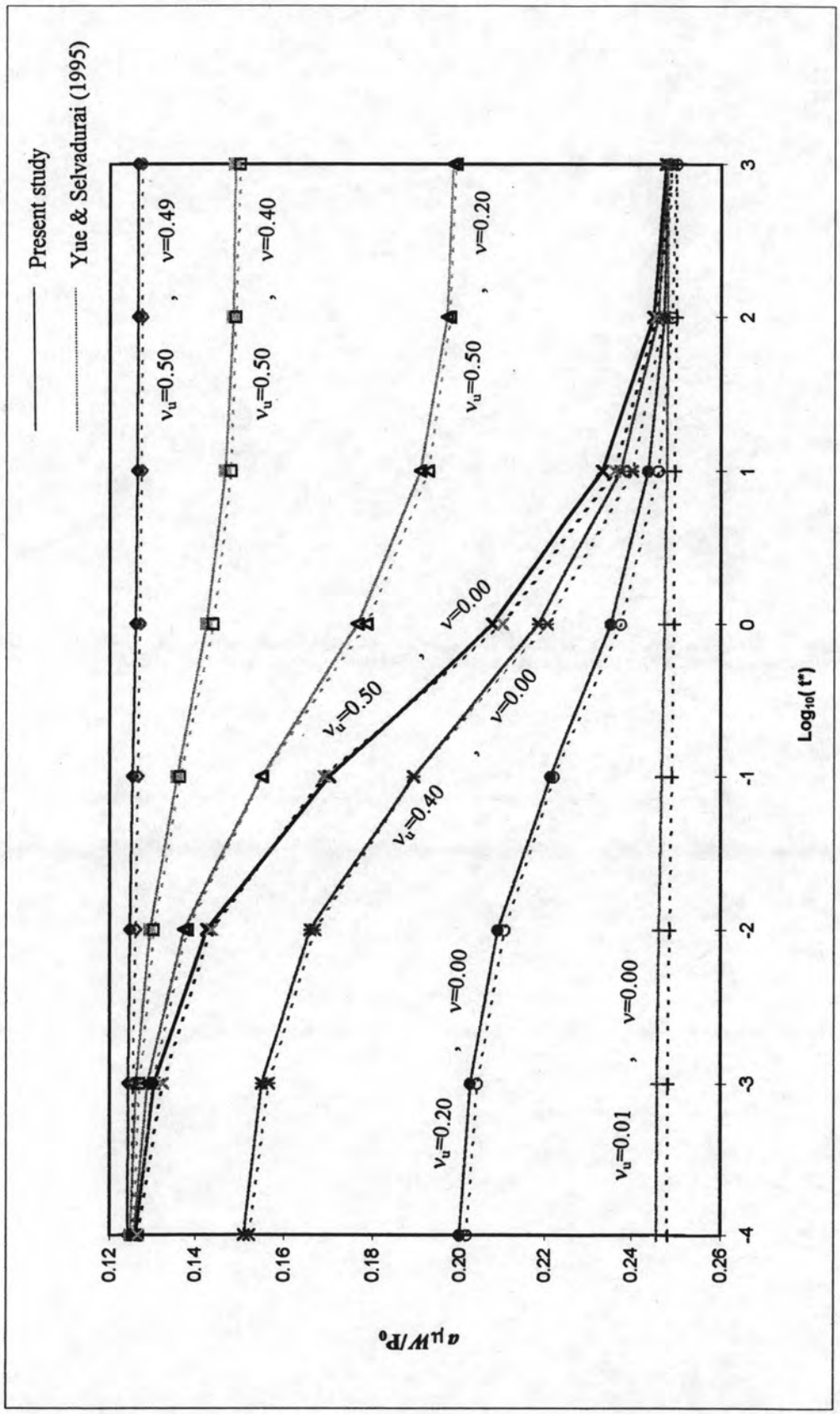

Figure 4.2 : Comparison of nondimensional displacement of rigid plate on homogeneous poroelastic half-space between the present study and Yue & Selvadurai (1995).

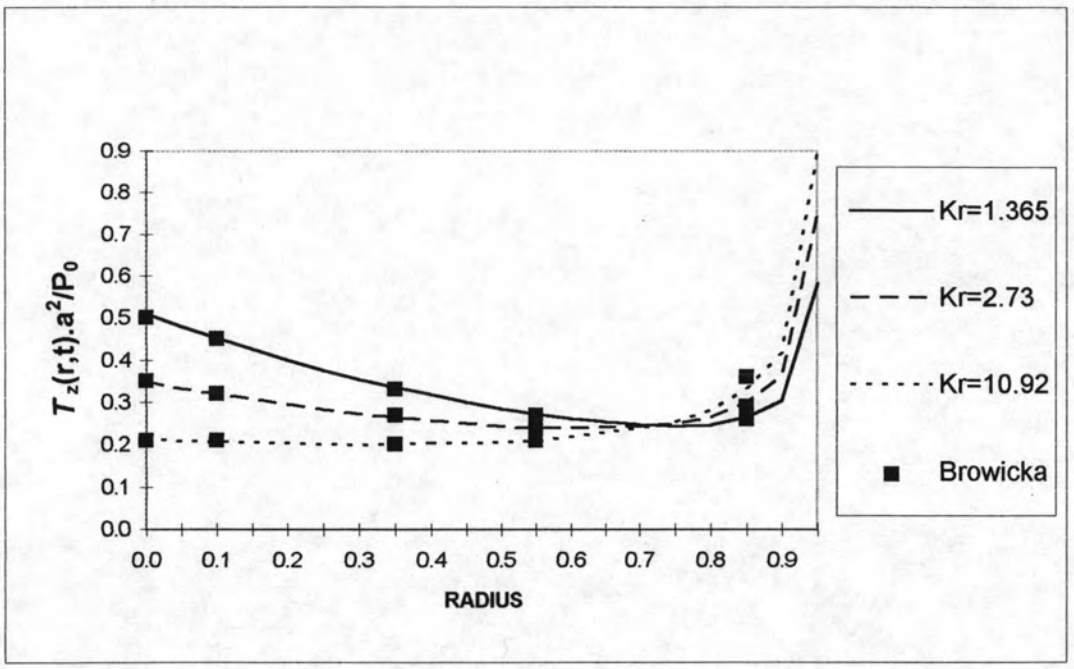

(a) Centrally loaded plate

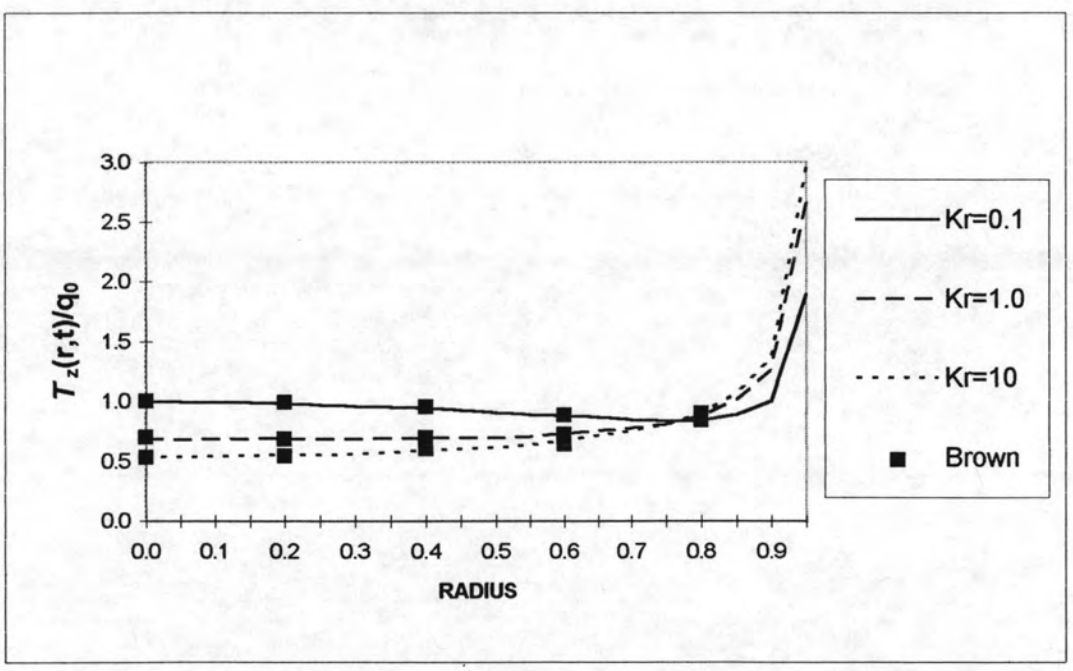

(b) Uniformly loaded plate

Figure 4.3 : Comparison of contact stress of circular elastic plate resting on homogeneous elastic half-space.

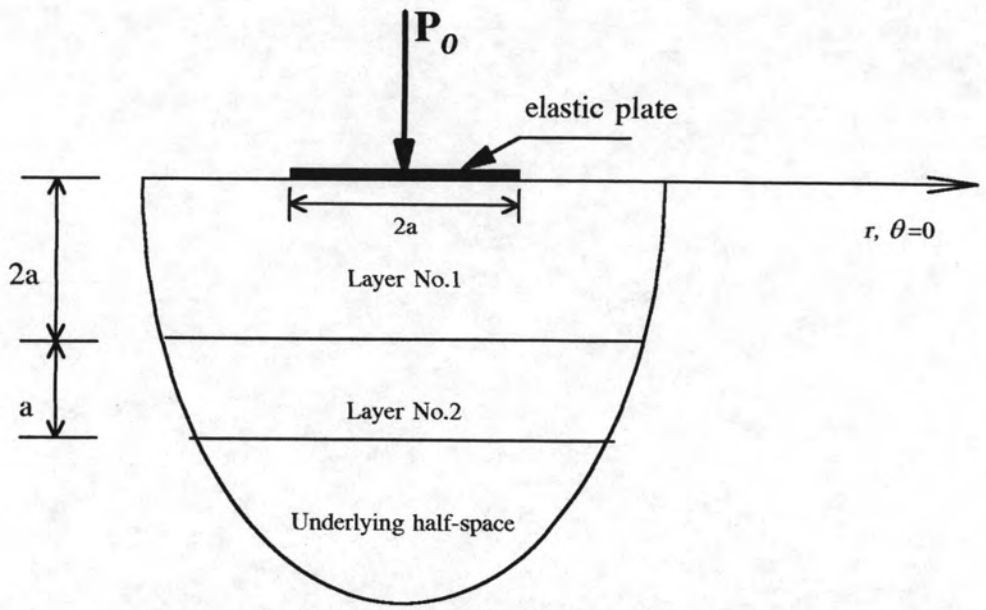

(a) Centrally loaded elastic plate

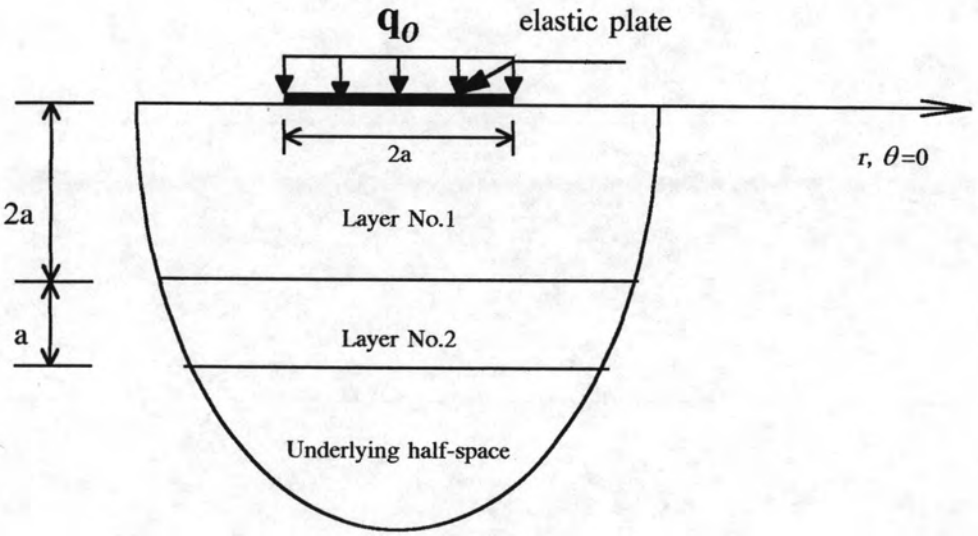

(b) Uniformly loaded elastic plate

Figure 4.4 : Circular elastic plate on multi-layered poroelastic half-space subjected to axisymmetric loadings considered in numerical study.

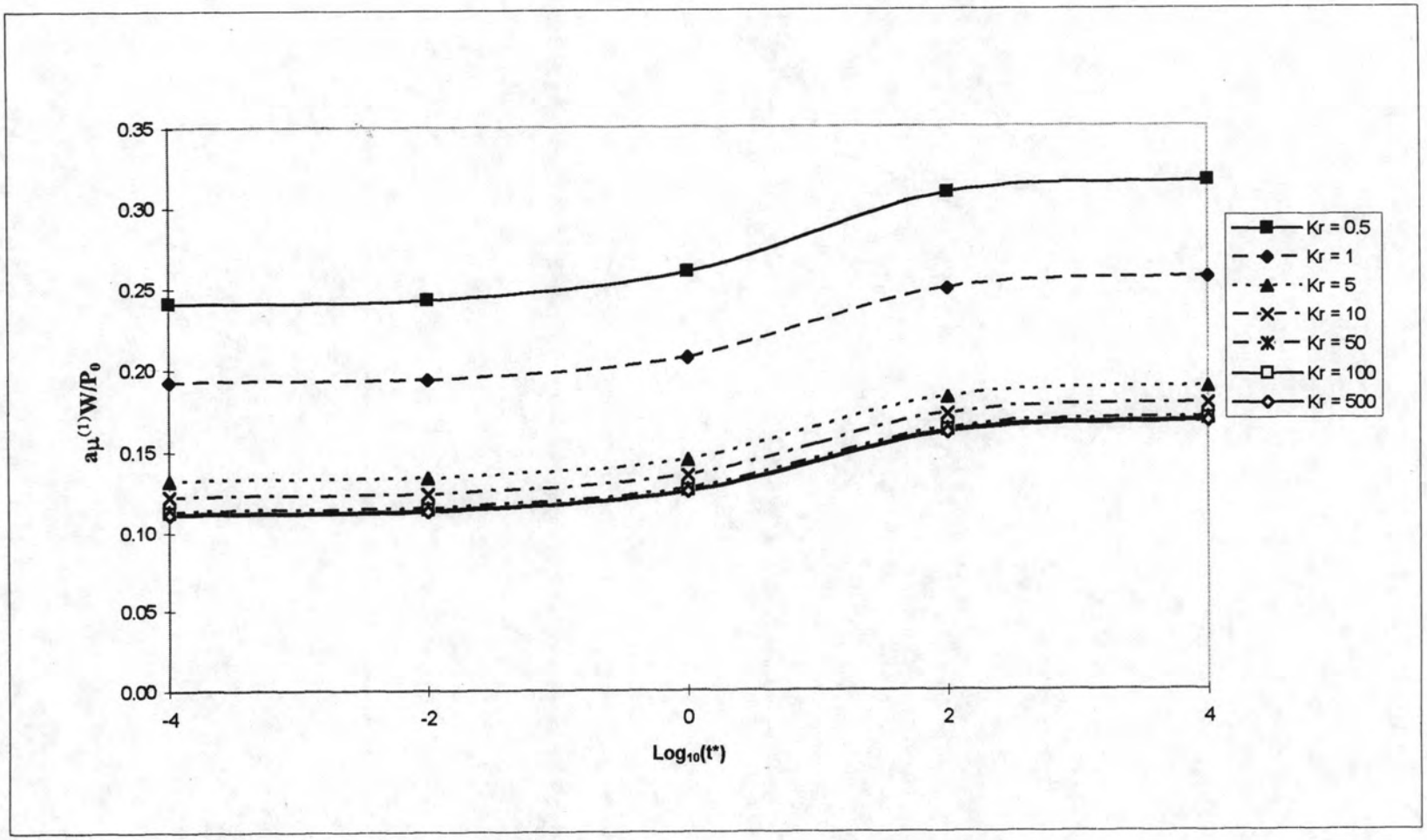

Figure 4.5 : Time histories of nondimensional displacement at r=0 of centrally loaded plate on multi-layered poroelastic half-space for different Kr.

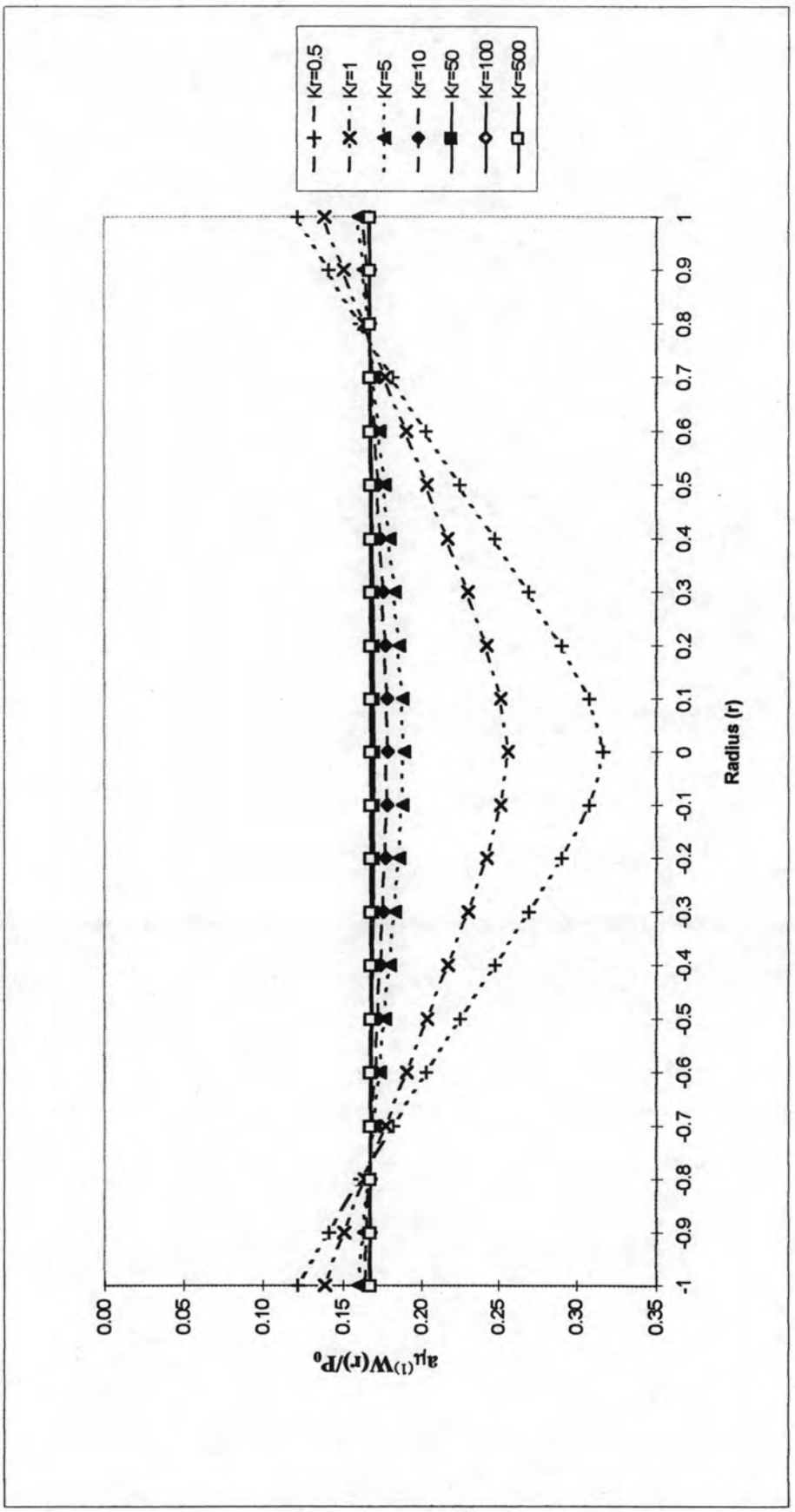

Figure 4.6 : Final deflected shape of centrally loaded elastic plate on multi-layered poroelastic half-space for different Kr.

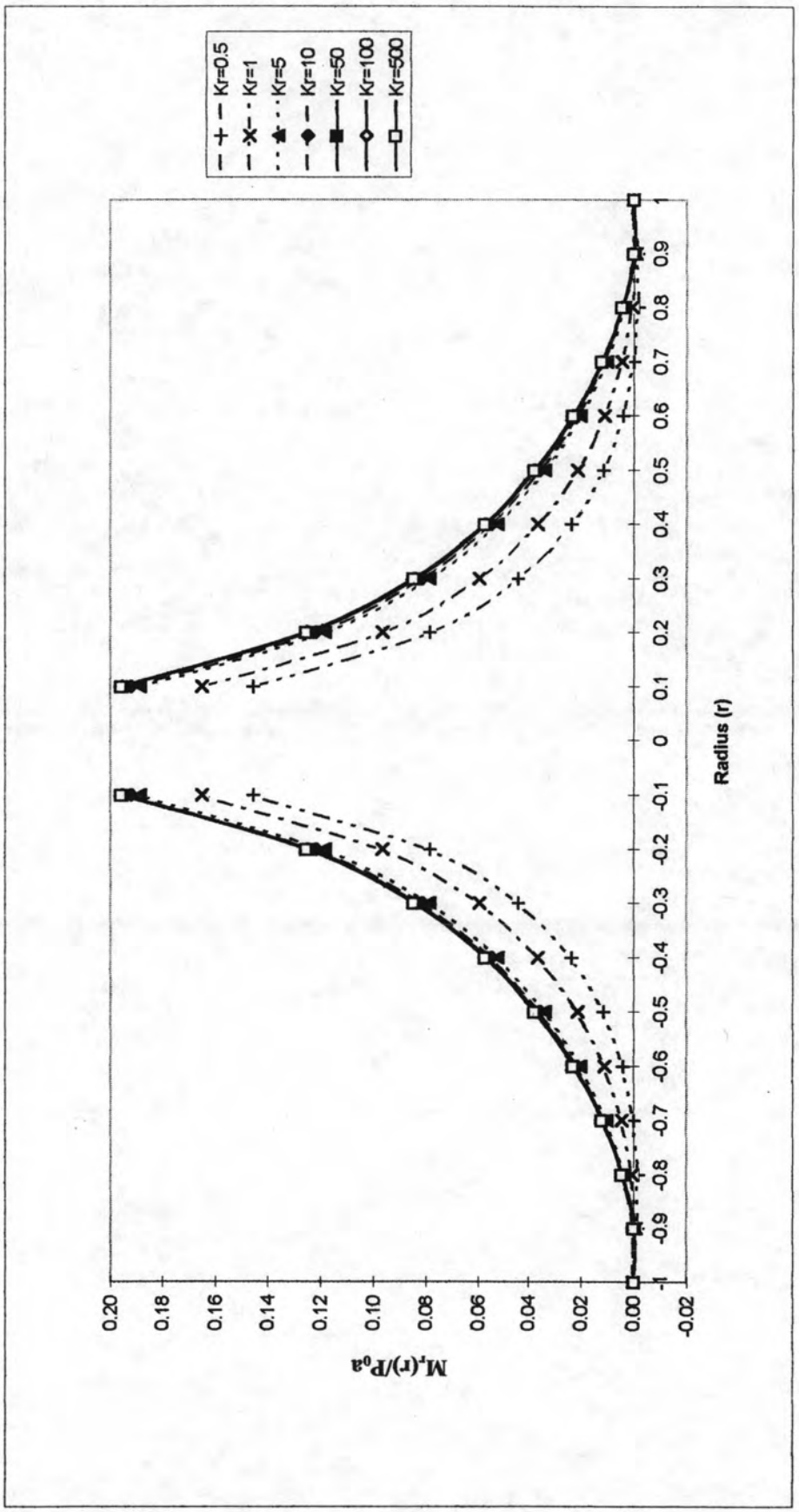

Figure 4.7 : Final solutions for nondimensional moment of centrally loaded elastic plate on multi-layered poroelastic half-space for different Kr.

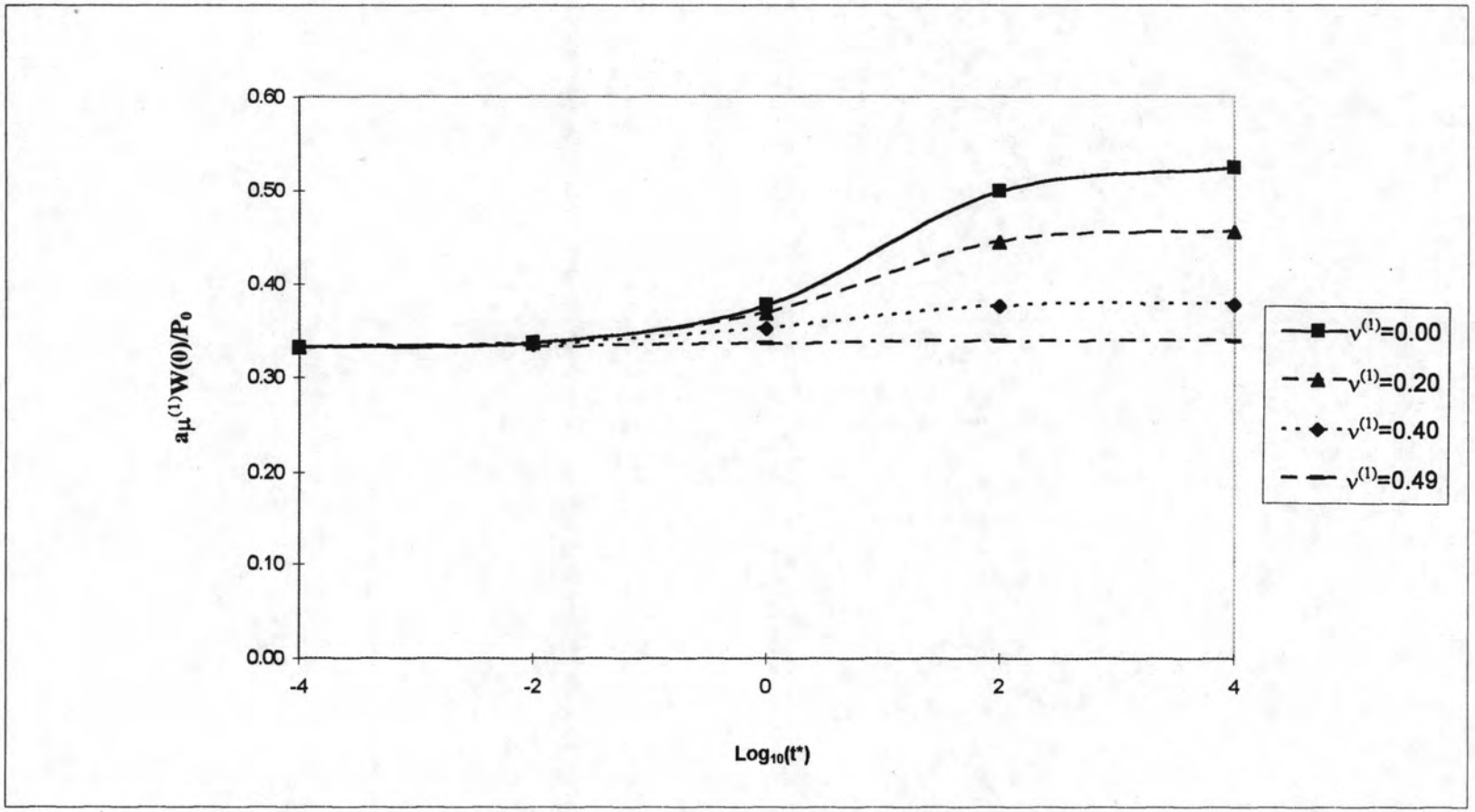

Figure 4.8 : Time histories of nondimensional displacement at r=0 of centrally loaded elastic plate on multi-layered poroelastic half-space for different $\nu^{(1)}$.

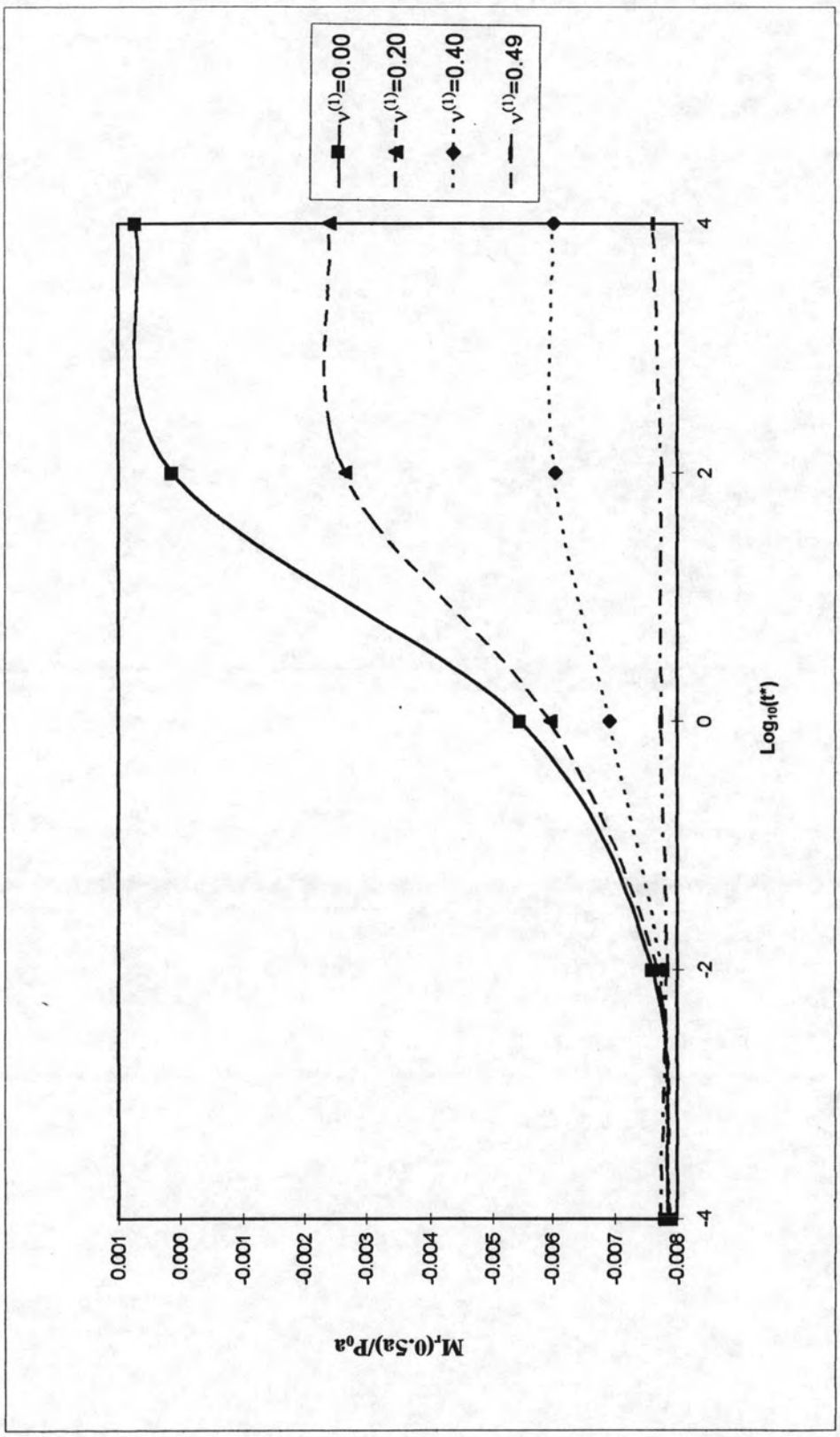

Figure 4.9 : Time histories of nondimensional moment at r=0.5a of centrally loaded elastic plate on multi-layered poroelastic half-space for different $\nu^{(1)}$.

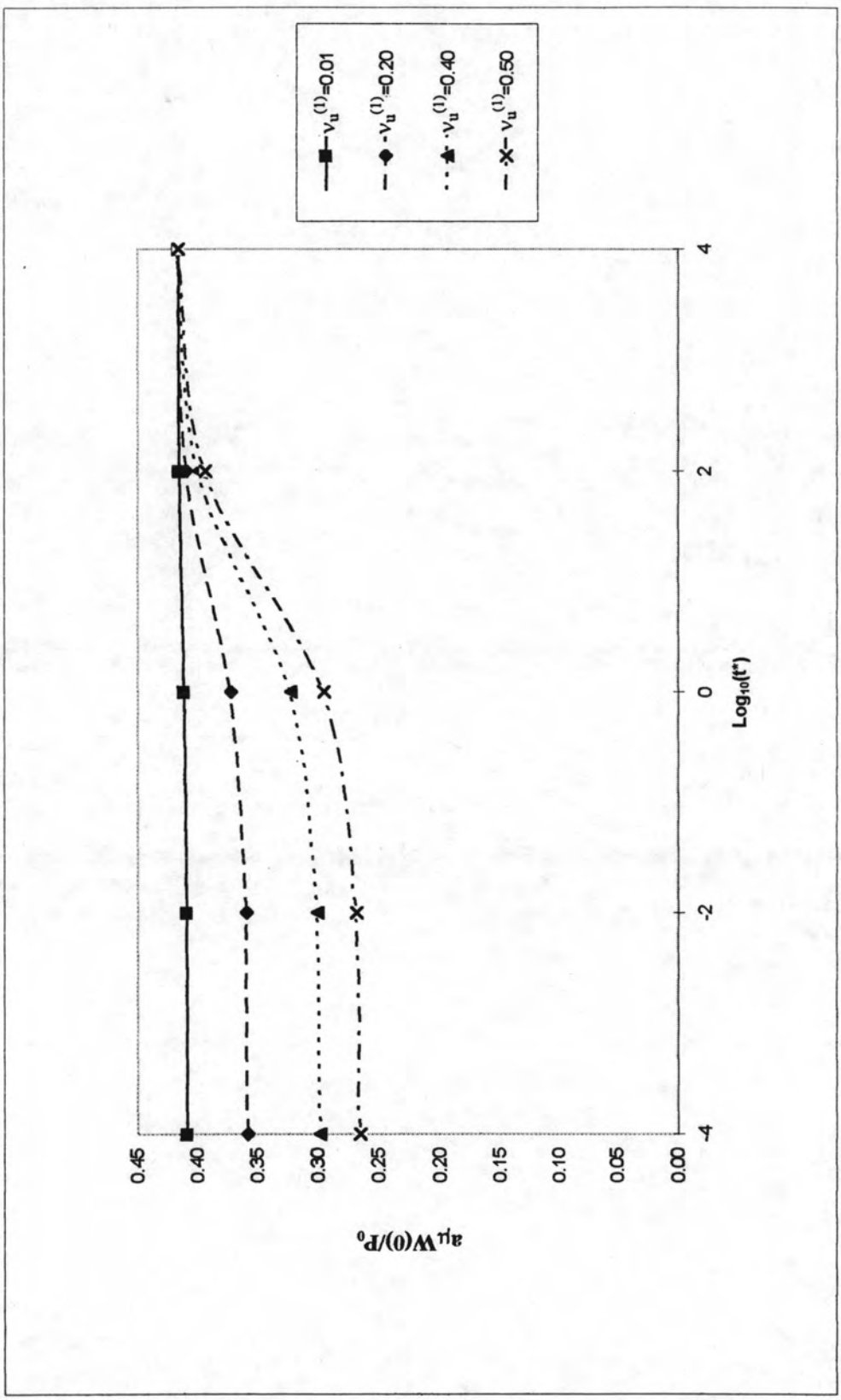

Figure 4.10 : Time histories of nondimensional displacement at r=0 of centrally loaded elastic plate on multi-layered poroelastic half-space for different $\nu_u^{(1)}$.

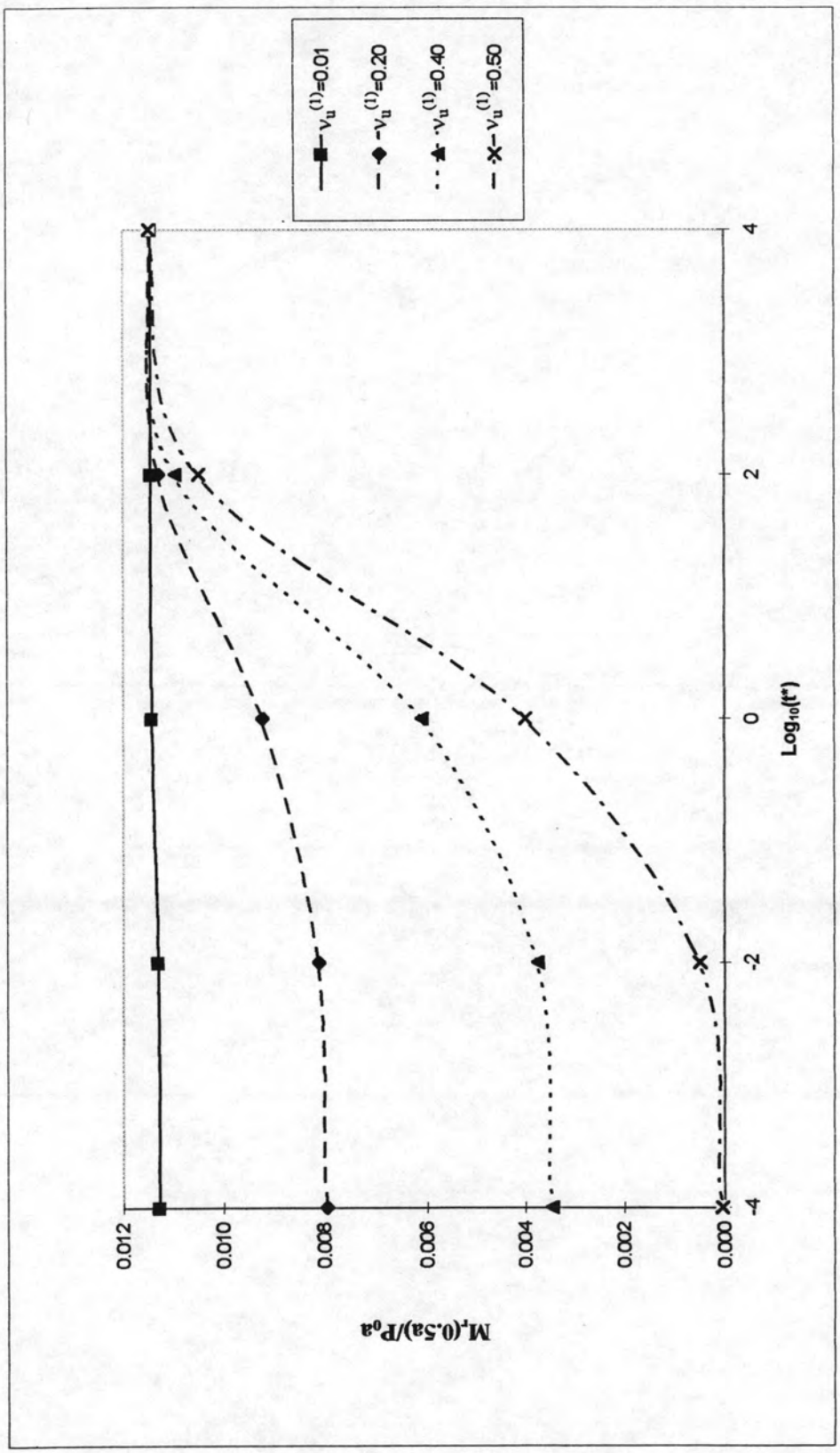

Figure 4.11 : Time histories of nondimensional moment at r=0.5a of centrally loaded elastic plate on multi-layered poroelastic half-space for different $\nu_u^{(1)}$.

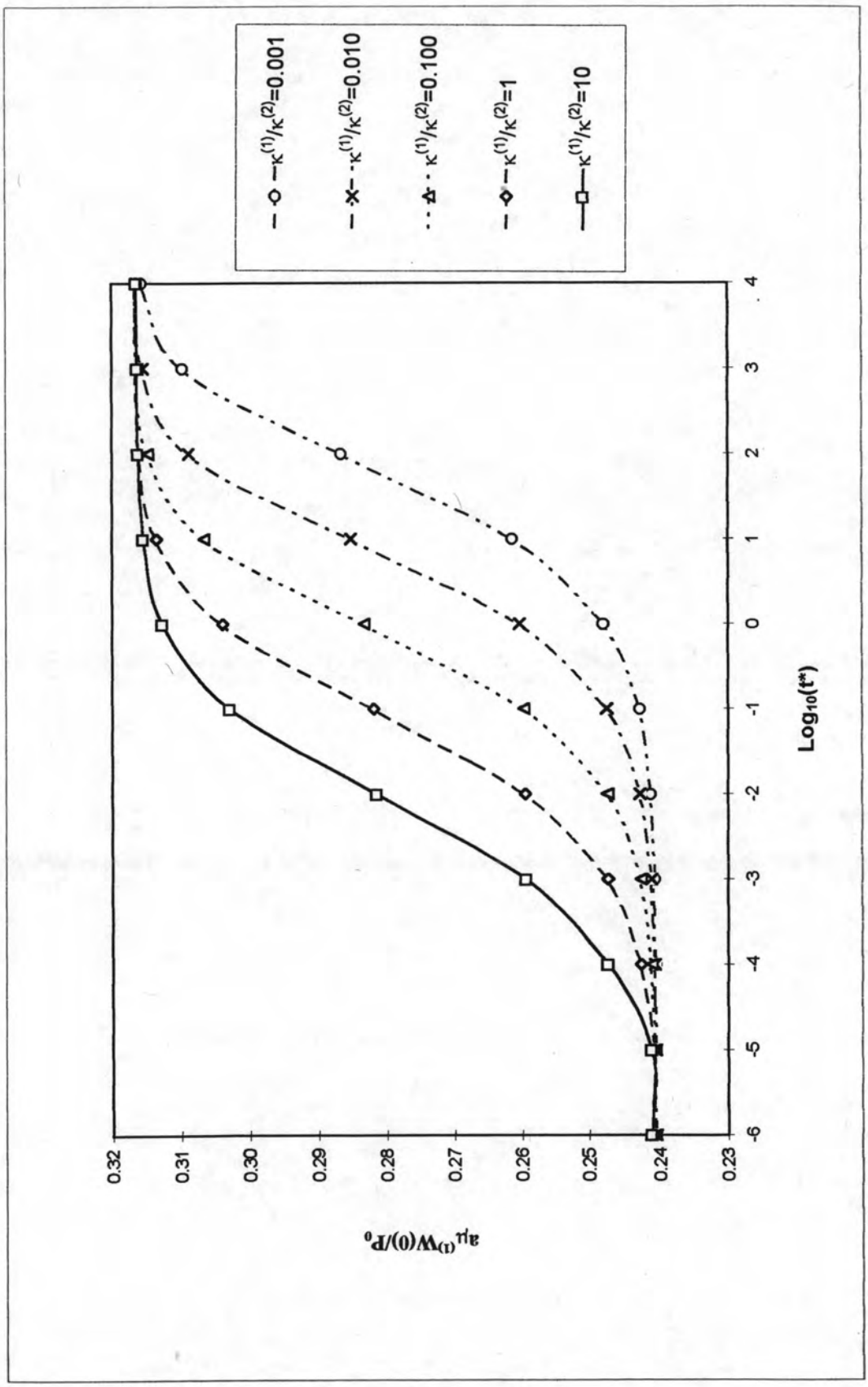

Figure 4.12 : Time histories of nondimensional displacement at r=0 of centrally loaded elastic plate on multi-layered poroelastic half-space for different $\kappa^{(1)}/\kappa^{(2)}$.

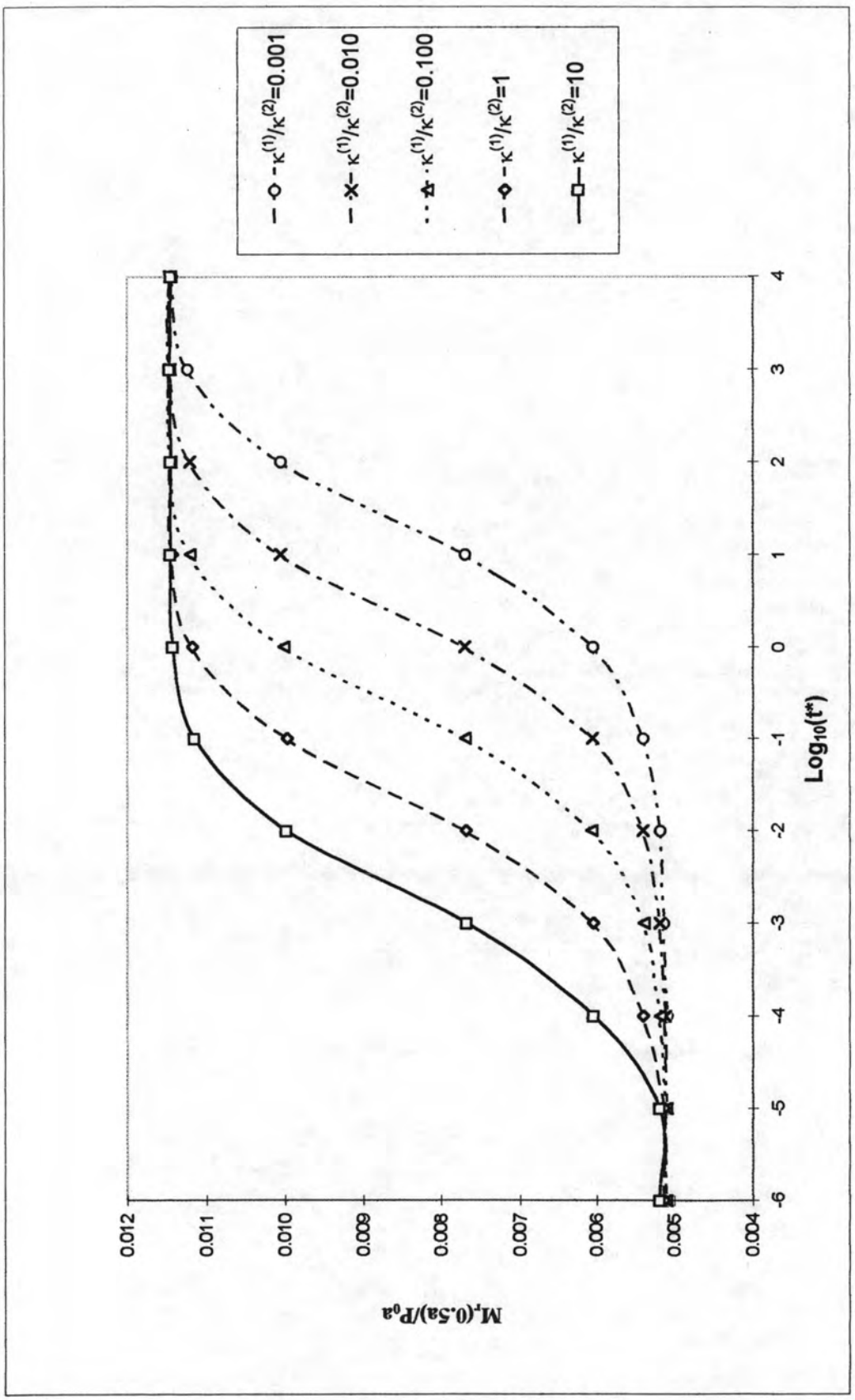

Figure 4.13 : Time histories of nondimensional moment at r=0.5a of centrally loaded elastic plate on multi-layered poroelastic half-space for different $\kappa^{(1)}/\kappa^{(2)}$.

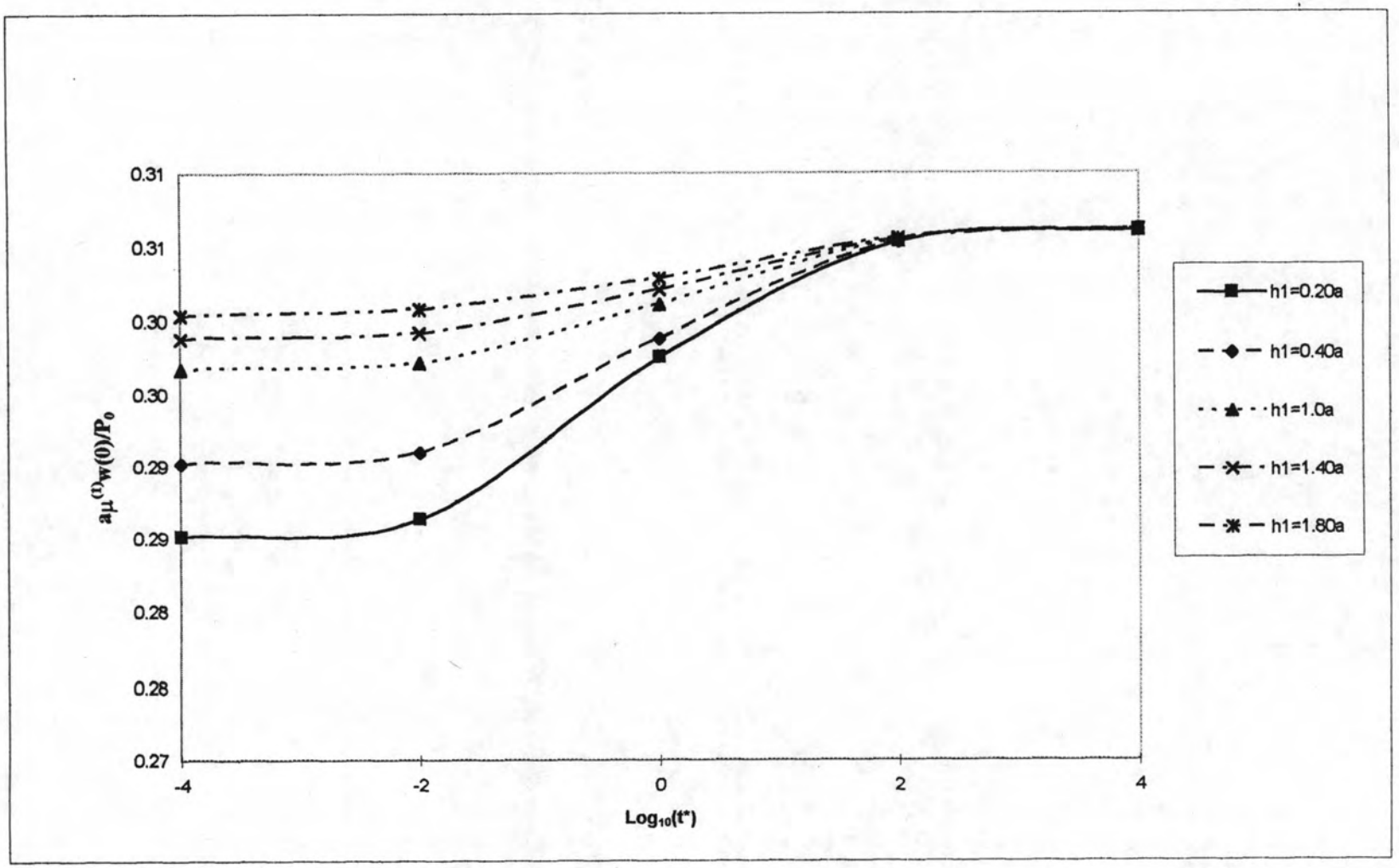

Figure 4.14 : Time histories of nondimensional displacement at r=0 of centrally loaded elastic plate on multi-layered poroelastic half-space for different h1 .

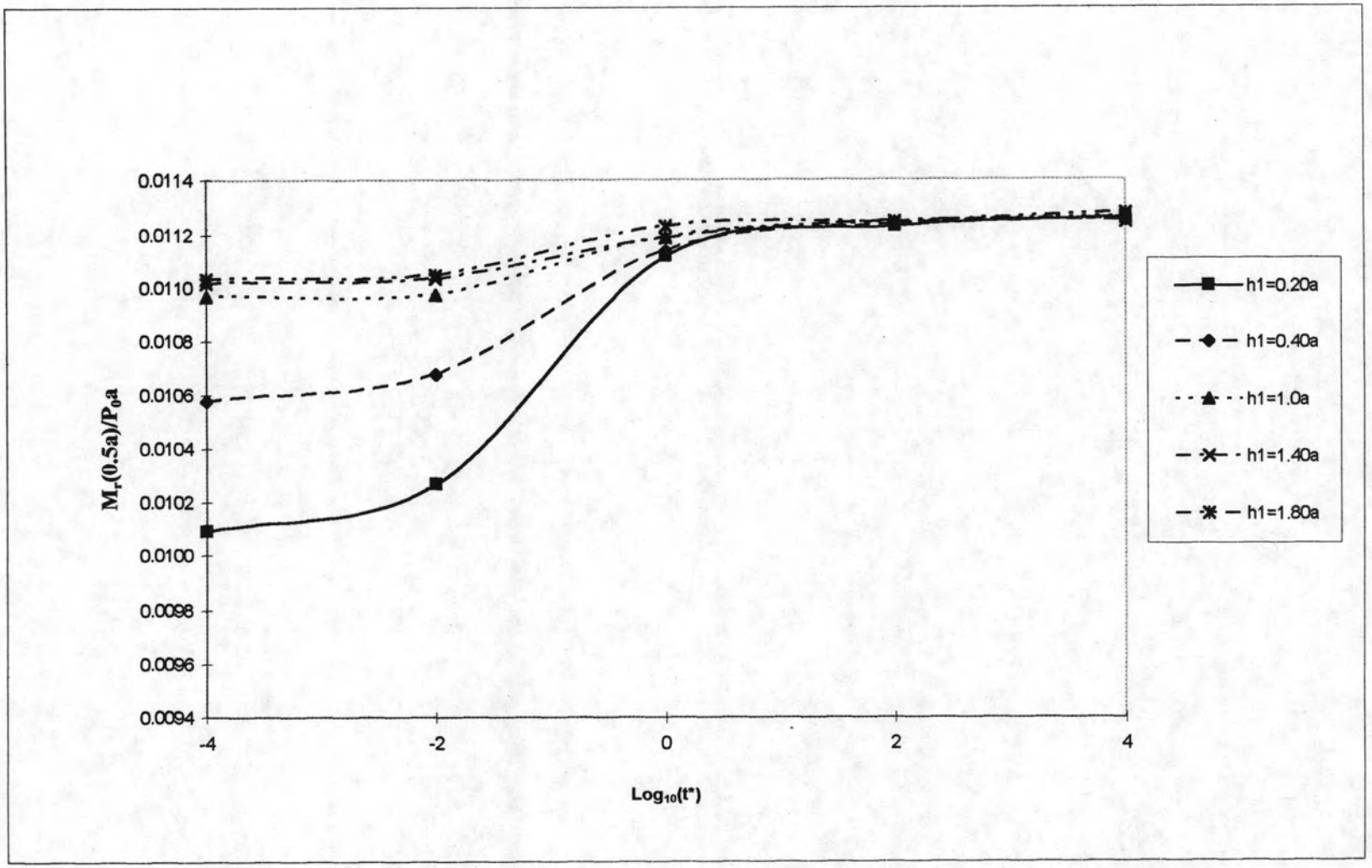

Figure 4.15 : Time histories of nondimensional moment at r=0.5a of centrally loaded elastic plate on multi-layered poroelastic half-space for different h1 .

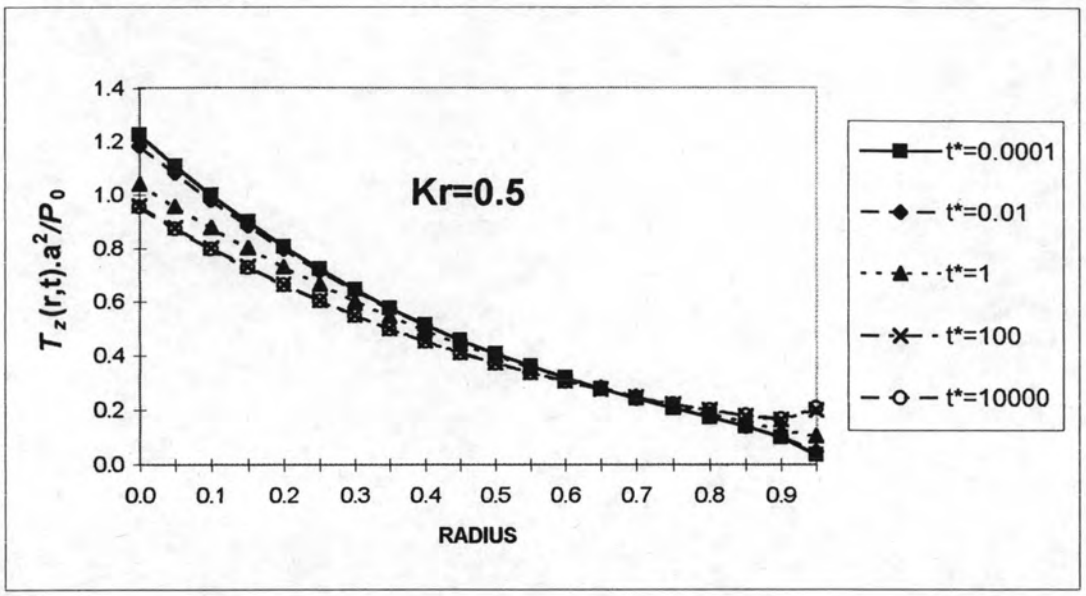

(a)

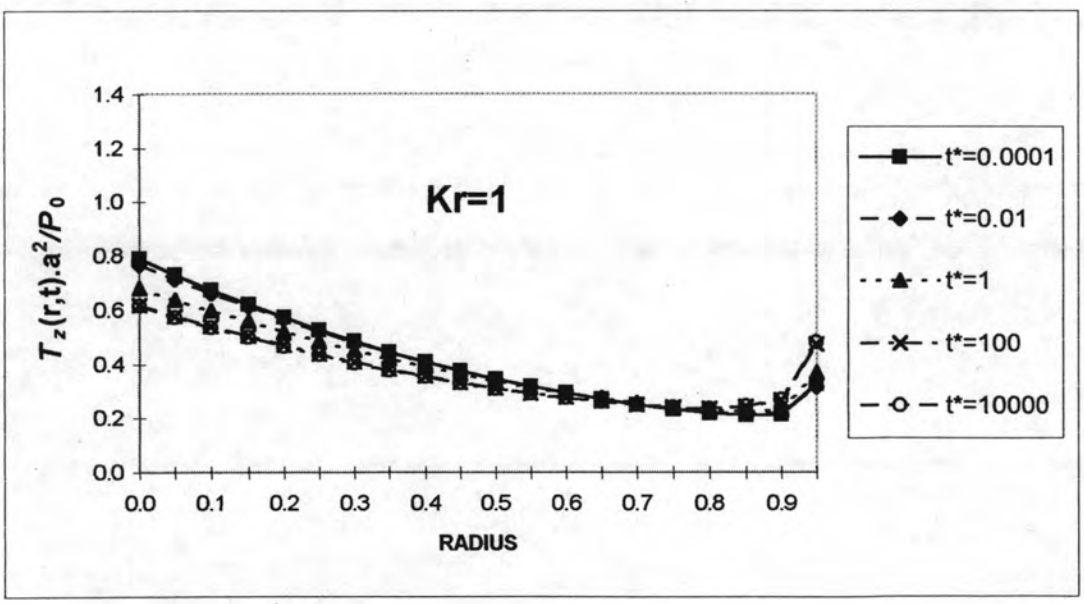

(b)

Figure 4.16 : Contact stress of centrally loaded elastic plate on multi-layered poroelastic half-space for different Kr and t^*

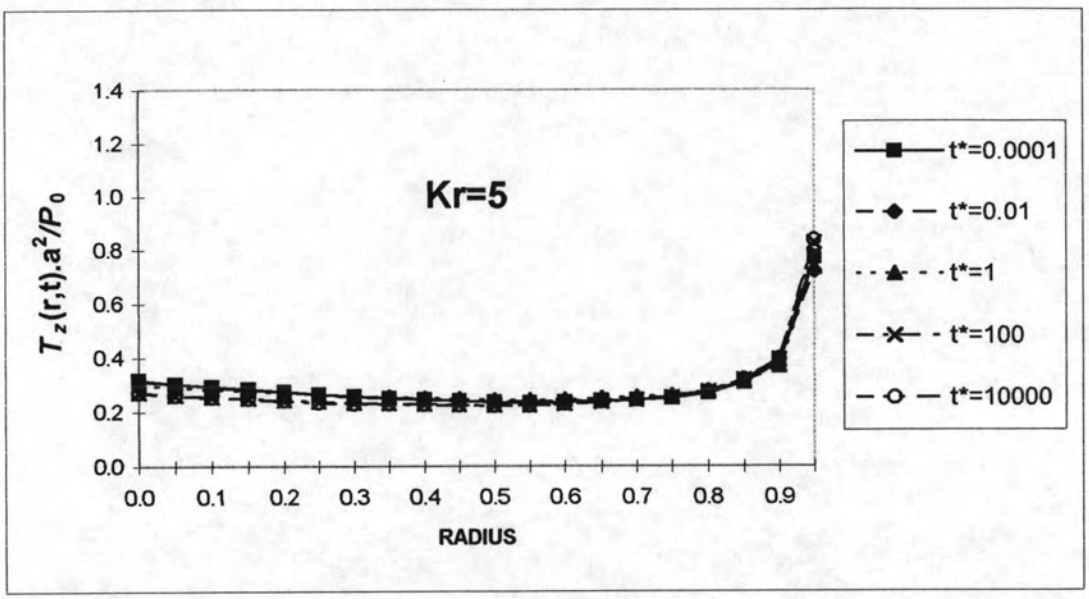

(c)

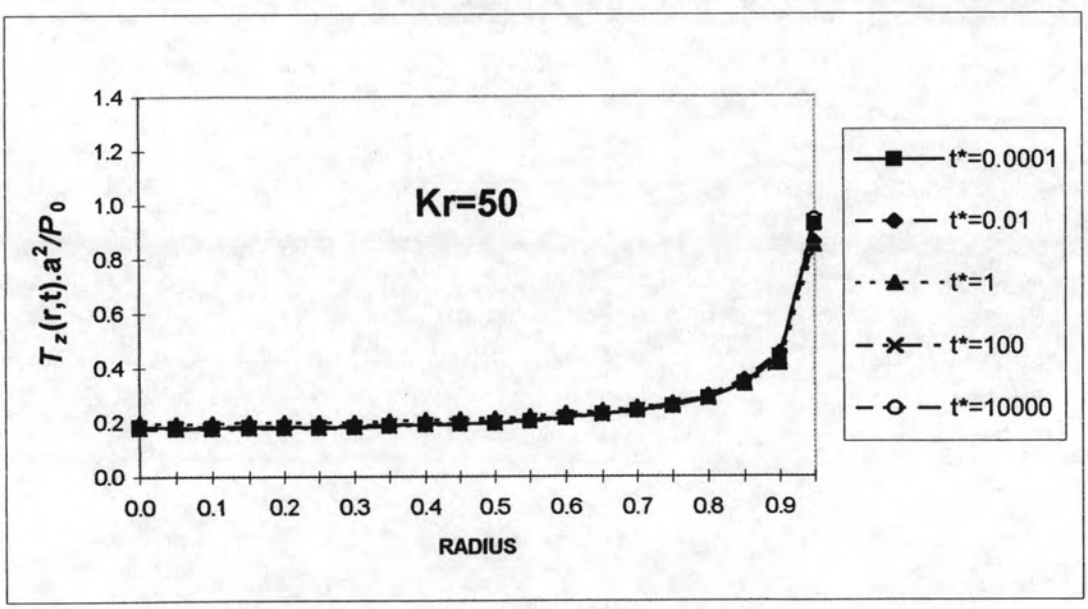

(d)

Figure 4.16 : Contact stress of centrally loaded elastic plate on multi-layered poroelastic half-space for different Kr and t^*

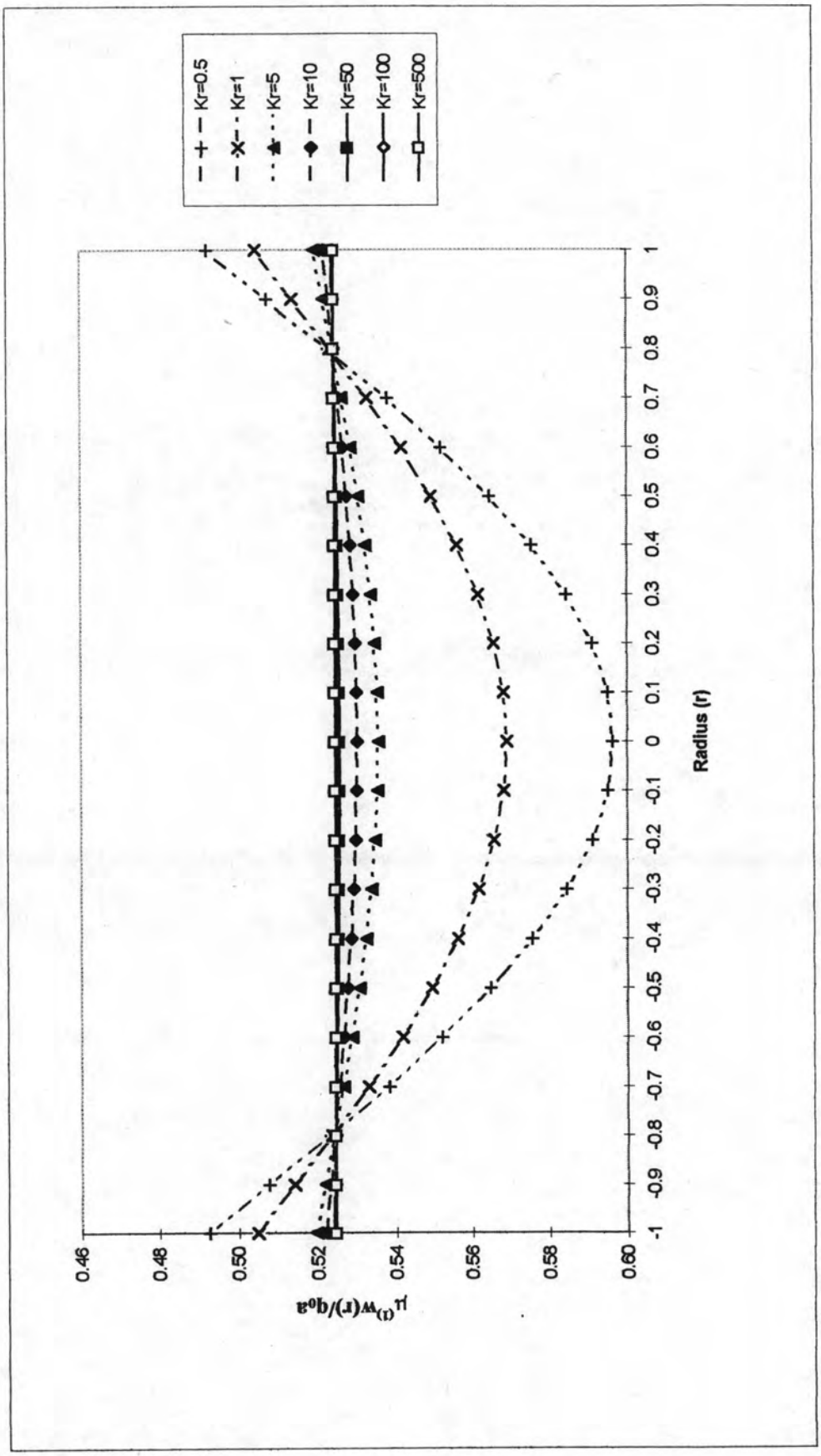

Figure 4.17 : Final deflected shape of uniformly loaded elastic plate on multi-layered poroelastic half-space for different Kr.

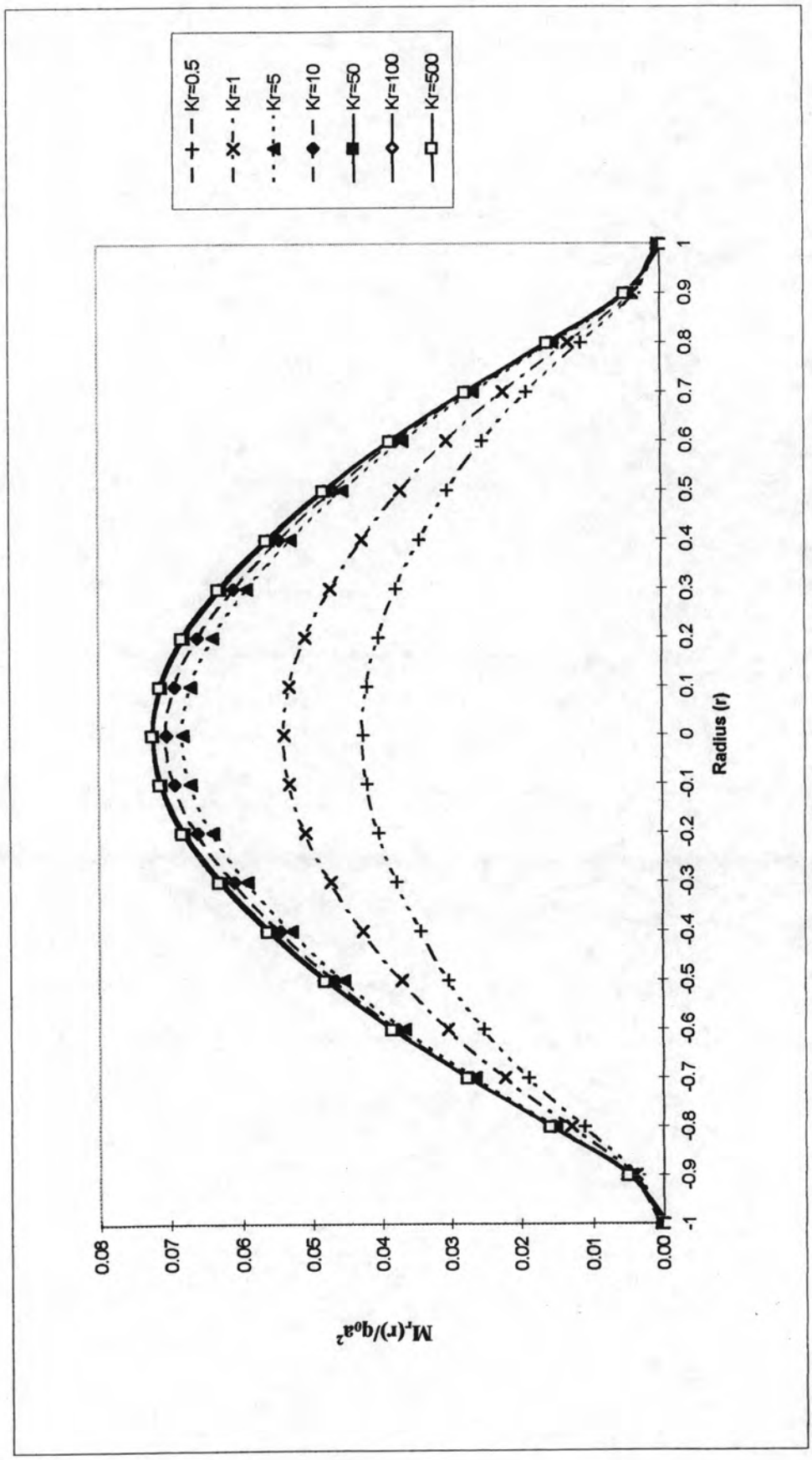

Figure 4.18 : Final solutions for nondimensional moment of uniformly loaded elastic plate on multi-layered poroelastic half-space for different Kr.

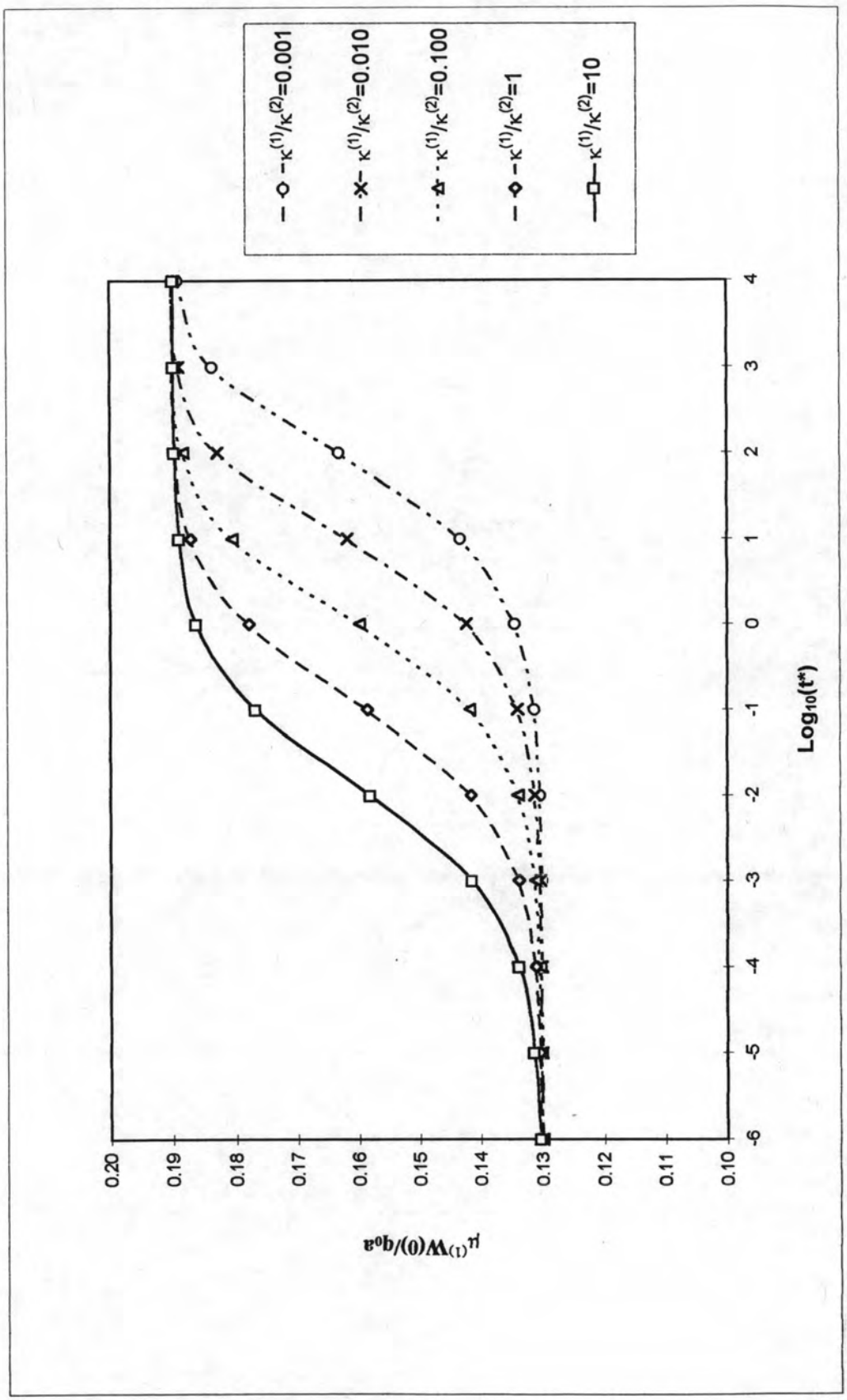

Figure 4.19 : Time histories of nondimensional displacement at r=0 of uniformly loaded elastic plate on multi-layered poroelastic half-space for different $\kappa^{(1)}/\kappa^{(2)}$.

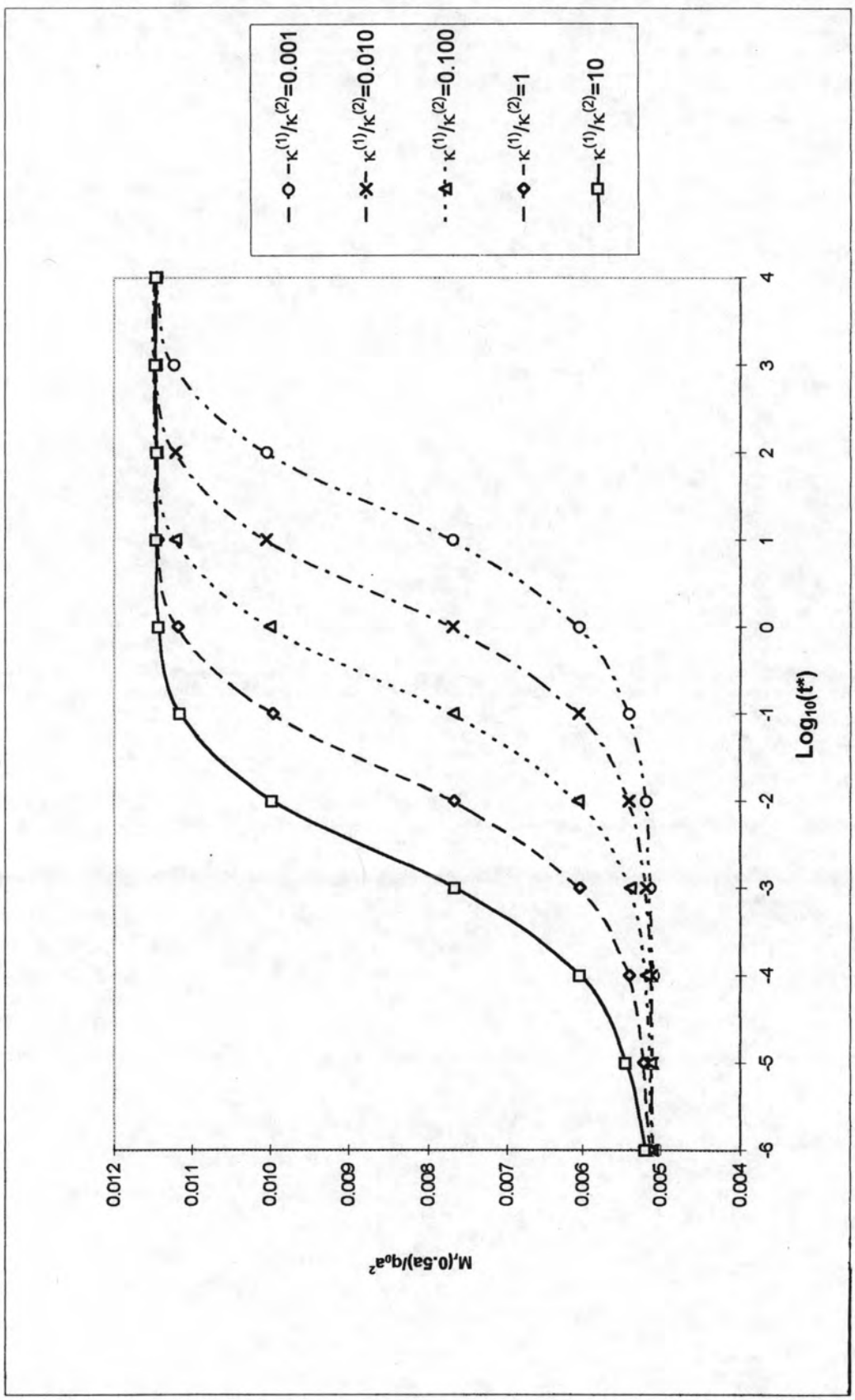

Figure 4.20 : Time histories of nondimensional moment at r=0.5a of uniformly loaded elastic plate on multi-layered poroelastic half-space for different $\kappa^{(1)}/\kappa^{(2)}$.

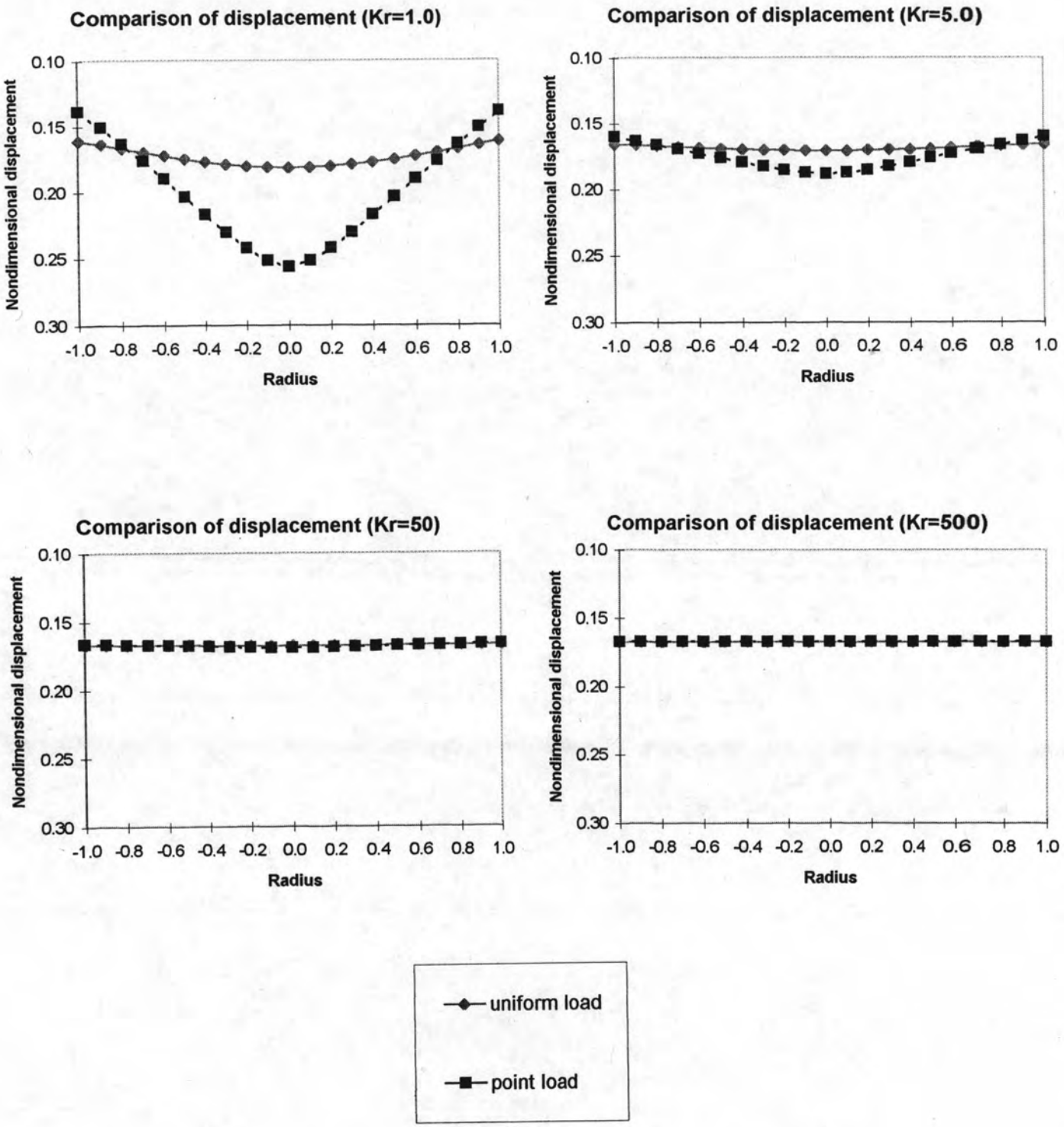

Figure 4.21 : Comparison of final deflected shape between centrally loaded plate and uniformly loaded plate for different Kr.

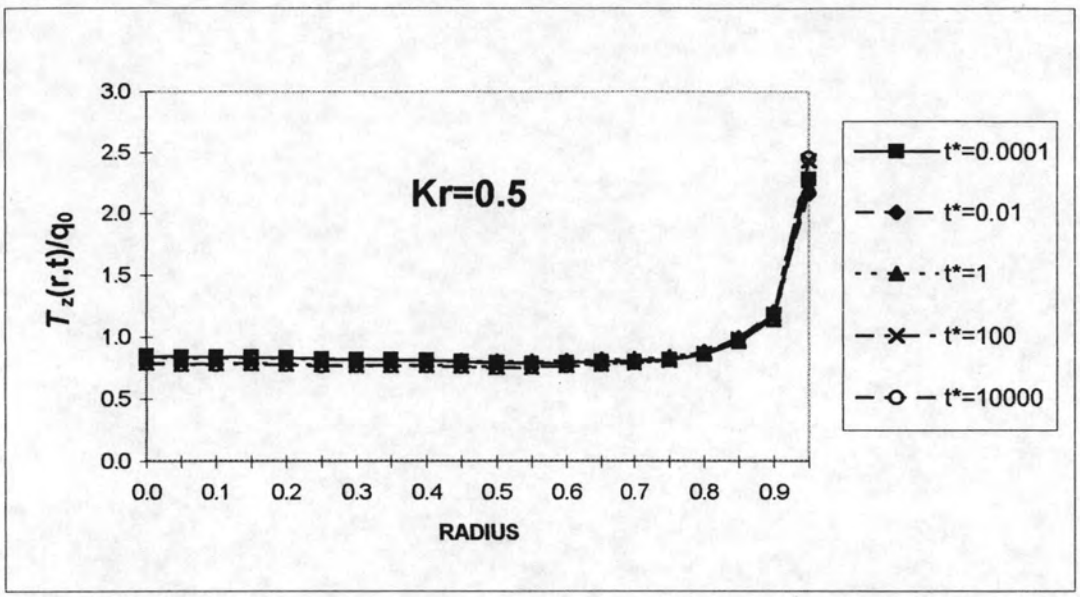

(a)

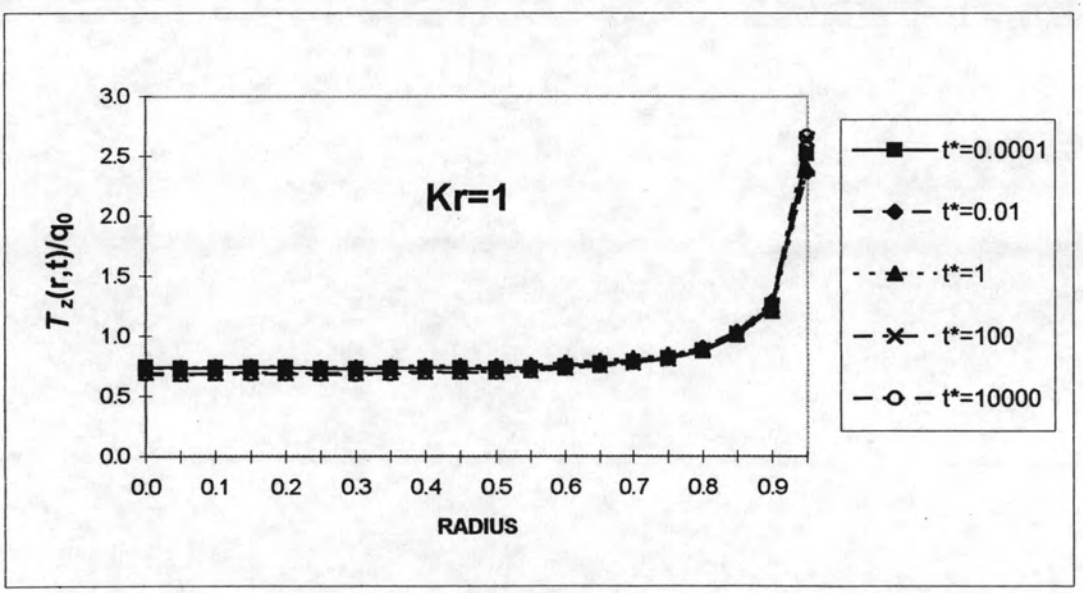

(b)

Figure 4.22 : Contact stress of uniformly loaded elastic plate on multi-layered poroelastic half-space for different Kr and t^*

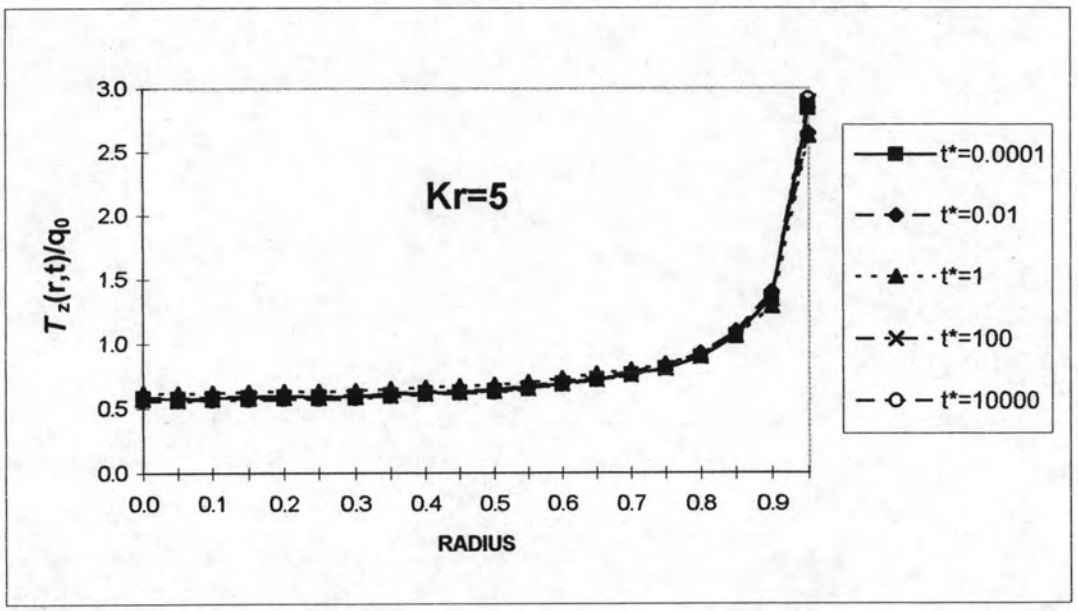

(c)

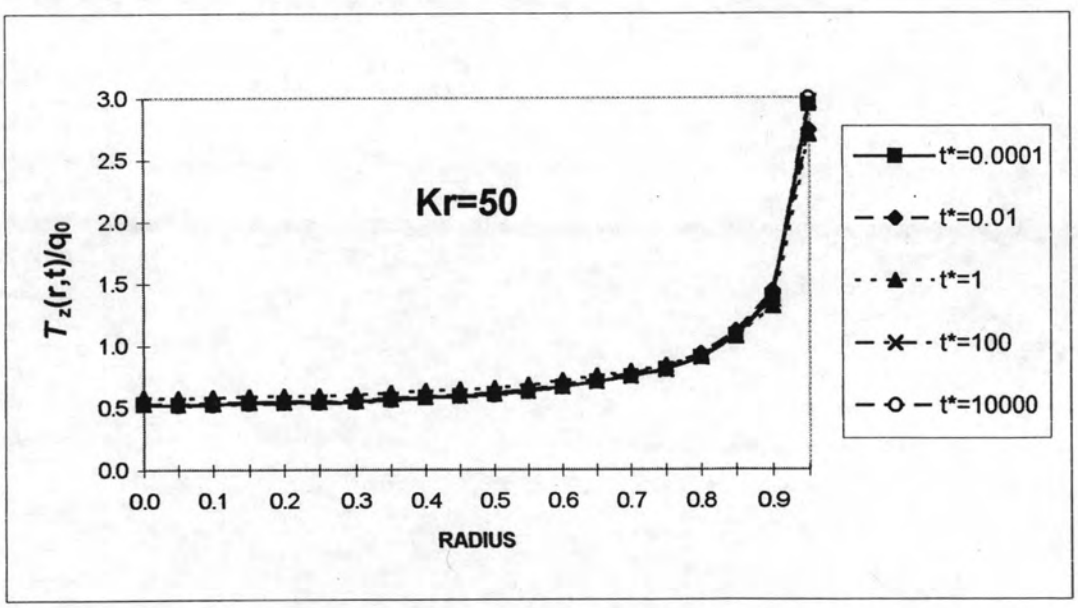

(d)

Figure 4.22 : Contact stress of uniformly loaded elastic plate on multi-layered poroelastic half-space for different Kr and t^*